

# MINCE

## II. Neutron capture elements<sup>★</sup>

P. François<sup>1,2</sup>, G. Cescutti<sup>3,4,5</sup>, P. Bonifacio<sup>1</sup>, E. Caffau<sup>1</sup>, L. Monaco<sup>6</sup>, M. Steffen<sup>7</sup>, J. Puschner<sup>8</sup>,  
F. Calura<sup>9</sup>, S. Cristallo<sup>10,11</sup>, P. Di Marcantonio<sup>4</sup>, V. Dobrovolskas<sup>12</sup>, M. Franchini<sup>4</sup>, A. J. Gallagher<sup>7</sup>,  
C. J. Hansen<sup>13</sup>, A. Korn<sup>8</sup>, A. Kučinskas<sup>12</sup>, R. Lallemand<sup>4</sup>, L. Lombardo<sup>13</sup>, F. Lucertini<sup>14</sup>, L. Magrini<sup>15</sup>,  
A. M. Matas Pinto<sup>1</sup>, F. Matteucci<sup>3,4,5</sup>, A. Mucciarelli<sup>16,9</sup>, L. Sbordone<sup>14</sup>, M. Spite<sup>1</sup>,  
E. Spitoni<sup>4</sup>, and M. Valentini<sup>7</sup>

<sup>1</sup> GEPI, Observatoire de Paris, Université PSL, CNRS, 5 Place Jules Janssen, 92190 Meudon, France  
e-mail: patrick.francois@obspm.fr

<sup>2</sup> UPJV, Université de Picardie Jules Verne, Pôle Scientifique, 33 rue St Leu, 80039 Amiens, France

<sup>3</sup> Dipartimento di Fisica, Sezione di Astronomia, Università di Trieste, Via G. B. Tiepolo 11, 34143 Trieste, Italy

<sup>4</sup> INAF, Osservatorio Astronomico di Trieste, Via Tiepolo 11, 34143 Trieste, Italy

<sup>5</sup> INFN, Sezione di Trieste, Via A. Valerio 2, 34127 Trieste, Italy

<sup>6</sup> Instituto de Astrofísica, Departamento de Ciencias Físicas, Universidad Andres Bello, Autopista Concepcion-Talcahuano 7100, Chile

<sup>7</sup> Leibniz-Institut für Astrophysik Potsdam (AIP), An der Sternwarte 16, 14482 Potsdam, Germany

<sup>8</sup> Division of Astronomy and Space Physics, Department of Physics and Astronomy, Uppsala University, Box 516, 75120 Uppsala, Sweden

<sup>9</sup> INAF – Osservatorio di Astrofisica e Scienza dello Spazio di Bologna, Via Gobetti 93/3, 40129 Bologna, Italy

<sup>10</sup> INAF, Osservatorio Astronomico d'Abruzzo, Via Mentore Maggini snc, 64100 Teramo, Italy

<sup>11</sup> INFN, Sezione di Perugia, Via A. Pascoli snc, 06123 Perugia, Italy

<sup>12</sup> Institute of Theoretical Physics and Astronomy, Vilnius University, Saulėtekio al. 3, Vilnius 10257, Lithuania

<sup>13</sup> Goethe University Frankfurt, Institute for Applied Physics, Max-von-Laue-Str. 12, 60438 Frankfurt am Main, Germany

<sup>14</sup> ESO-European Southern Observatory, Alonso de Cordova 3107, Vitacura, Santiago, Chile

<sup>15</sup> INAF, Osservatorio Astrofisico di Arcetri, Largo E. Fermi 5, 50125 Firenze, Italy

<sup>16</sup> Dipartimento di Fisica e Astronomia, Università degli Studi di Bologna, Via Gobetti 93/2, 40129 Bologna, Italy

Received 8 February 2024 / Accepted 26 March 2024

### ABSTRACT

**Context.** Most of the studies on the determination of the chemical composition of metal-poor stars have been focused on the search of the most pristine stars, searching for the imprints of the ejecta of the first supernovae. Apart from the rare and very interesting r-enriched stars, few elements are measurable in the very metal-poor stars. On the other hand, a lot of work has been done also on the thin-disc and thick-disc abundance ratios in a metallicity range from  $[\text{Fe}/\text{H}] > -1.5$  dex to solar. In the available literature, the intermediate metal-poor stars ( $-2.5 < [\text{Fe}/\text{H}] < -1.5$ ) have been frequently overlooked. The MINCE (Measuring at Intermediate metallicity Neutron-Capture Elements) project aims to gather the abundances of neutron-capture elements but also of light elements and iron peak elements in a large sample of giant stars in this metallicity range. The missing information has consequences for the precise study of the chemical enrichment of our Galaxy in particular for what concerns neutron-capture elements and it will be only partially covered by future multi object spectroscopic surveys such as WEAVE and 4MOST.

**Aims.** The aim of this work is to study the chemical evolution of galactic sub-components recently identified (i.e. *Gaia* Sausage Enceladus (GSE), Sequoia).

**Methods.** We used high signal-to-noise ratios, high-resolution spectra and standard 1D LTE spectrum synthesis to determine the detailed abundances.

**Results.** We could determine the abundances for up to 10 neutron-capture elements (Sr, Y, Zr, Ba, La, Ce, Pr, Nd, Sm and Eu) in 33 stars. The general trends of abundance ratios [n-capture element/Fe] versus  $[\text{Fe}/\text{H}]$  are in agreement with the results found in the literature. When our sample is divided in sub-groups depending on their kinematics, we found that the run of  $[\text{Sr}/\text{Ba}]$  versus  $[\text{Ba}/\text{H}]$  for the stars belonging to the GSE accretion event shows a tight anti-correlation. The results for the Sequoia stars, although based on a very limited sample, shows a  $[\text{Sr}/\text{Ba}]$  systematically higher than the  $[\text{Sr}/\text{Ba}]$  found in the GSE stars at a given  $[\text{Ba}/\text{H}]$  hinting at a different nucleosynthetic history. Stochastic chemical evolution models have been computed to understand the evolution of the GSE chemical composition of Sr and Ba. The first conclusions are that the GSE chemical evolution is similar to the evolution of a dwarf galaxy with galactic winds and inefficient star formation.

**Conclusions.** Detailed abundances of neutron-capture elements have been measured in high-resolution, high signal-to-noise spectra of intermediate metal-poor stars, the metallicity range covered by the MINCE project. These abundances have been compared to detailed stochastic models of galactic chemical evolution.

**Key words.** stars: abundances – stars: atmospheres – Galaxy: abundances – Galaxy: evolution – Galaxy: halo

\* Based on observations made with HARPSN at TNG, Fies at NOT, Sophie at OHP and ESPaDOnS at CFHT.

## 1. Introduction

The MINCE (Measuring at Intermediate metallicity Neutron-Capture Elements) project aims to gather abundances for the neutron-capture elements of several hundred stars at intermediate metallicity using different facilities worldwide. The idea is to study the nucleosynthetic signatures that can be found in old stars, in particular in the specific class of chemical elements with  $Z > 30$ ; that is, the neutron-capture elements. As neutron-capture elements are formed through several nucleosynthetic channels (mainly the s-process and the r-process), they can be used to constrain their source of production throughout the history of the Galaxy. In particular, it will be possible to determine the spread in the neutron-capture elements as a function of metallicity, revealing the different sites of production of the r-process that has enriched the interstellar medium at different timescales (Cescutti et al. 2008, 2015; Simonetti et al. 2019).

While most of the observational efforts have been put into the search for the most metal-poor stars, several detailed analyses (Ishigaki et al. 2013; Roederer et al. 2014) have considered the full range of metallicities, including the stars in the intermediate range of metallicity between the most metal-poor ones ( $[\text{Fe}/\text{H}] < -2.5$ ) and thin- or thick-disc stars ( $[\text{Fe}/\text{H}] > -1.5$ ).

The interest in analysing stars in this metallicity range is that the determination of their detailed abundance ratios is associated with accurate kinematics derived from the *Gaia* Early Data Release 3 (EDR3; Gaia Collaboration 2016, 2021). This information can be used to constrain the most recent models of galactic chemical evolution but can also help to characterise the recently discovered stellar streams and galactic substructures (see e.g. Belokurov et al. 2018; Haywood et al. 2018; Helmi et al. 2018; Myeong et al. 2019; Kruijssen et al. 2020; Naidu et al. 2020; Malhan et al. 2021; Feuillet et al. 2021, and reference therein). Although the SAGA database (Suda et al. 2008) reveals that the study of the chemical composition of stars in the intermediate metallicity range has also been well covered, the aim of our project is to analyse a large sample of stars in the same metallicity range using the same methods (codes, a line list, the derivation of stellar parameters, and so on) to derive chemical abundances, with the aim of deriving a set of homogeneous abundances.

This paper follows the article of Cescutti et al. (2022, hereafter MINCE I). In their paper, the authors present the first sample of 46 stars. They measured radial velocities and computed Galactic orbits for all of the stars. They found that eight stars belong to the thin disc and 15 to disrupted satellites, and that the remaining ones cannot be associated with the aforementioned structures; they call the latter halo stars. For 33 stars, they provided abundances of a set of elements up to zinc. This article presents the results of the determination of the abundances for up to ten neutron-capture elements using the same set of reduced spectra.

The paper is structured as follows. In Sect. 2, we present the main characteristics of the spectra that have been used in this study. In Sect. 3, we provide details of the lines that were used to compute the abundances. Section 4 gives a summary on how the stellar parameters were determined, and discusses the method used to compute the abundances and their associated errors. In this section, we also show how some elemental abundances are affected by non-local thermodynamic equilibrium (NLTE) effects. In Sect. 5, we present the results of the abundance determinations and a comparison with the literature data. Section 6 shows a comparison between the abundance ratios found in *Gaia*-Sausage-Enceladus (GSE, Belokurov et al. 2018;

Haywood et al. 2018; Helmi et al. 2018) and Sequoia (Barbá et al. 2019; Villanova et al. 2019; Myeong et al. 2019) in light of the recent abundance results from Aguado et al. (2021) and Matsuno et al. (2022). Detailed models of galactic chemical evolution for the GSE substructure are presented in Sect. 7. Finally, Sect. 8 summarises the main conclusions that can be drawn from this first set of MINCE data.

## 2. Dataset

As more detailed information is given in MINCE I, we recall the main characteristics of the dataset in this section. Spectra were taken with several instruments that deliver high-resolution spectra. From lower to higher spectral resolution, we have:

- ESPaDOnS (Donati et al. 2006) is a fibre-fed spectro-polarimeter installed on the 3.6m Canada-France-Hawaii telescope (CFHT) at Mauna Kea Observatory. The observing mode used (star + sky) gives a resolving power of  $R = 65\,000$  and the spectral range extends from 370 nm to 1051 nm.

- FIES (Telting et al. 2014) is a fibre-fed cross-dispersed high-resolution echelle spectrograph with a maximum spectral resolution of  $R = 67\,000$  installed at the Nordic Optical Telescope (NOT), which is a 2.56-m telescope located at the Roque de los Muchachos Observatory in Canarias. The spectral range is 370–830 nm.

- The Sophie spectrograph (Bouchy & Sophie Team 2006), installed on the Observatoire de Haute Provence (OHP) 1.93 m telescope, has been used in high-resolution mode, providing a resolving power of  $R = 75\,000$  and a spectral range from 387.2 nm to 694.3 nm.

- HARPS-N (Cosentino et al. 2012) is a high-resolution spectrograph with a resolving power  $R = 115\,000$  and spectral coverage ranging from 383 to 693 nm. The spectrograph is installed at the 3.58 m Telescopio Nazionale Galileo (TNG) at the Roque de Los Muchachos Observatory.

As was mentioned in the first paper of the series (MINCE I), the spectra were obtained thanks to a total of four proposals with three different Principle Investigators: Cescutti for HARPS-north at TNG, E. Spitoni for FIES at NOT, and P. Bonifacio for Sophie at OHP and ESPaDOnS at CFHT.

## 3. Line list

In the spectra of this work, we could identify the lines of ten neutron-capture elements. In order to have a complete description of the lines used in our analysis, we report below the sources of the oscillator strengths and hyperfine structure (HFS) if present for a given element.

**Strontium.** We first selected the three ionised strontium lines at 4077.71 Å, 4161.79 Å, and 4215.52 Å, and the Sr I line at 4607.33 Å. Given that the stars in our sample are giant stars and that the metallicity range is between  $\approx$  solar and  $[\text{Fe}/\text{H}] \approx -2.5$  dex, the Sr II lines are saturated and the placement of the continuum is difficult to evaluate. We find that the Sr I line is a better choice over this range of stellar parameters.

**Yttrium.** Yttrium abundances were determined by fitting the Y II lines 4854.86 Å, 4883.68 Å, 4900.12 Å, 5087.42 Å, 5119.11 Å, 5123.21 Å, 5200.41 Å, 5402.77 Å, and 5662.93 Å. We adopted the oscillator strengths computed by Hannaford et al. (1982).

**Zirconium.** The Zr II lines at 4317.30 Å, 4613.95 Å, 5112.27 Å, and 5350.35 Å were used to determine its abundance. The log  $gf$ s are from [Ljung et al. \(2006\)](#).

**Barium.** We used the Ba II lines at 5853.68 Å, 6141.71 Å, and 6496.90 Å to derive the Barium abundances. Hyperfine splitting and isotopic shifts were taken into account, following [Gallagher et al. \(2020\)](#). The isotopic fractions for isotopes 134, 135, 136, 137, and 138 are the r-process fractions 0%, 40%, 0%, 32%, and 28% respectively, following [McWilliam \(1998\)](#).

**Lanthanum.** The La II lines at 4662.51 Å, 4920.98 Å, 4921.78 Å, 5114.56 Å, 5122.99 Å, and 5290.82 Å were used. The log  $gf$ 's are from [Lawler et al. \(2001\)](#). Hyperfine structure was taken from [Ivans et al. \(2006\)](#).

**Cerium.** The Ce II lines at 4539.85 Å, 4562.28 Å, 4628.16 Å, and 5187.46 Å were used in this study. The log  $gf$ 's are from [Palmeri et al. \(2000\)](#).

**Praseodymium.** The Pr II abundances were determined using the Pr II lines at 5219.05 Å, 5220.11 Å, 5259.73 Å, 5322.76 Å, and 6165.89 Å. The oscillator strengths and HFS are from [Li et al. \(2007\)](#), [Ivarsson et al. \(2001\)](#), and [Snedden et al. \(2009\)](#).

**Neodymium.** The singly ionised transitions of neodymium (Nd II) at 4501.81 Å, 4859.03 Å, 4959.12 Å, 5076.58 Å, 5255.50 Å, 5293.16 Å, and 5319.81 Å were used to determine the neodymium abundance. The atomic data are from [Den Hartog et al. \(2003\)](#).

**Samarium.** The Sm II lines at 4566.20 Å, 4615.44 Å, 4669.64 Å, 4674.59 Å, 4676.90 Å, 4791.58 Å, and 4913.26 Å were used in this work. The log  $gf$ s were taken from [Lawler et al. \(2006\)](#). There are no HFSs available for these transitions. In any case, they would only affect the odd isotopes,  $^{147}\text{Sm}$  and  $^{149}\text{Sm}$ , which account for only about 29% of the Sm abundance in the Solar System.

**Europium.** The two Eu II lines at 4435.58 Å and 6645.10 Å were measured in our spectra. For a couple of stars, we could also measure the transition at 4522.58 Å. Atomic quantities such as oscillator strengths, HFS, and isotopic shifts were adopted from [Lawler et al. \(2001\)](#). We assumed a 50–50% mix for the Eu isotopes 151 and 153, following [Ivans et al. \(2006\)](#). We used `linemake`<sup>1</sup> to generate the line list for europium ([Placco et al. 2021](#)).

## 4. Analysis

### 4.1. Stellar parameters

The stellar parameters were taken from [MINCE I](#). To summarise, the stellar parameters were derived using colours and distances from *Gaia* EDR3 and de-reddened using the maps from [Schlafly & Finkbeiner \(2011\)](#); the process was iterated up to the point when the changes in stellar parameters were less than 50 K in  $T_{\text{eff}}$  and less than 0.05 dex in log  $g$ . For the micro-turbulence, we employed the calibration by [Mashonkina et al. \(2017\)](#) at any iteration, and applied these values as the final choice. The stellar parameters and derived metallicity are reported in Table 1.

**Table 1.** Stellar parameters of the sample.

Star	$T_{\text{eff}}$ (K)	log $g$ (gcs)	$\xi$ km s <sup>-1</sup>	[Fe/H]	$S/N$
HD 115575	4393	1.08	1.94	-1.99	88
TYC 4267-2023-1	4660	0.96	2.11	-1.74	68
BD+31 2143	4565	1.15	2.03	-2.37	100
BD+20 3298	4154	0.57	2.07	-1.95	92
TYC 1008-1200-1	4199	0.78	2.01	-2.23	50
HD 238439	4154	0.53	2.10	-2.09	87
HD 142614	4316	0.87	1.96	-1.46	95
BD+04 18	4053	0.74	1.9	-1.48	58
BD+39 3309	4909	1.73	1.94	-2.58	90
TYC 2824-1963-1	4036	0.64	1.95	-1.60	54
TYC 4001-1161-1	4129	0.75	1.94	-1.62	59
TYC 4221-640-1	4295	0.66	2.12	-2.27	54
TYC 4-369-1	4234	0.89	1.94	-1.84	50
BD-00 4538	4482	1.29	1.88	-1.9	99
BD+03 4904	4497	1.03	2.06	-2.58	58
BD+07 4625	4757	1.64	1.86	-1.93	98
BD+11 2896	4254	1.07	1.83	-1.41	85
BD+21 4759	4503	1.06	2.05	-2.51	60
BD+25 4520	4276	0.70	2.08	-2.28	98
BD+32 2483	4516	1.17	1.99	-2.25	88
BD+35 4847	4237	0.76	2.01	-1.92	84
BD+48 2167	4468	1.00	2.04	-2.29	99
BD-07 3523	4193	0.71	2.02	-1.95	84
BD+06 2880	4167	0.82	1.91	-1.45	74
HD 139423	4287	0.70	2.05	-1.71	83
HD 208316	4249	0.79	1.98	-1.61	90
HD 354750	4626	0.90	2.17	-2.36	83
TYC 2588-1386-1	4130	0.66	1.99	-1.74	50
TYC 3085-119-1	4820	2.26	1.56	-1.51	85
TYC 33-446-1	4289	0.75	2.07	-2.22	85
TYC 3944-698-1	4091	0.45	2.11	-2.18	50
TYC 4331-136-1	4133	0.50	2.13	-2.53	46
TYC 4584-784-1	4232	0.80	2.00	-2.04	40

**Notes.** Signal-to-noise ratios are given per resolution element at 500 nm.

### 4.2. Abundances

We carried out a classical 1D local thermodynamic equilibrium (LTE) analysis using `OSMARCS` model atmospheres ([Gustafsson et al. 1975, 2003, 2008](#); [Plez et al. 1992](#); [Edvardsson et al. 1993](#)). The abundances used in the model atmospheres were solar-scaled with respect to the [Grevesse & Sauval \(2000\)](#) solar abundances, except for the  $\alpha$  elements that are enhanced by 0.4 dex. We corrected the resulting abundances by taking into account the difference between the solar values of ([Grevesse & Sauval 2000](#)) and [Lodders et al. \(2009\)](#). The solar abundances we adopted are reported in Table 2.

The abundance analysis was performed using the LTE spectral line analysis code `turbospectrum` ([Alvarez & Plez 1998](#); [Plez 2012](#)), which treats scattering in detail. The abundances were determined by matching a synthetic spectrum centred on each line of interest to the observed one. Tables A.1 and A.2 list the lines used to measure the abundances in our sample of stars. Detailed HFS components have also been included in these tables. For the spectrum synthesis, we took into account all the known blending lines from the VALD database ([Ryabchikova et al. 2015](#), and references therein).

<sup>1</sup> <https://github.com/vmplacco/linemake>

**Table 2.** Solar abundances used throughout this paper are from [Lodders et al. \(2009\)](#).

Element	$A(X)$
Sr	2.90
Y	2.20
Zr	2.57
Ba	2.18
La	1.19
Ce	1.60
Pr	0.77
Nd	1.47
Sm	0.96
Eu	0.53

When not specified, we adopted the abundance derived from Fe I lines as the metallicity. Since our surface gravities are derived from the parallaxes and not the Fe ionisation equilibrium, in order to minimise the gravity dependence in abundance ratios, we used  $[X/Fe] = [X/Fe I]$ , where X is a neutral species and  $[X/Fe] = [X/Fe II]$  for ionised species.

#### 4.3. Non-local thermodynamic equilibrium effects

Strontium, barium, and europium are known to be sensitive to departures from LTE (or NLTE effects), particularly in metal-poor stars.

In this study, we used the Sr I strontium line at 4607.33 Å. The abundance of strontium in metal-poor stars has been studied in detail by [Hansen et al. \(2013\)](#). They confirmed that the ionisation equilibrium between Sr I and Sr II is satisfied in NLTE but not in LTE, where the difference between neutral and ionised Sr is on average  $-0.3$  dex. We applied a correction of  $-0.3$  dex on our Sr I result to match the literature results that are mostly based on Sr II lines. We note that we used the Sr I line because the Sr II lines visible in our spectra are saturated and the placement of the continuum is difficult to evaluate.

[Mashonkina et al. \(2008\)](#) computed the NLTE effect on barium and europium abundances in the metal-poor giant HD 122563 ( $[Fe/H] \approx -2.6$  dex), a metallicity at the lower end of our sample. Based on the Ba II lines at 4554.031 Å and 6496.90 Å, they derived a correction (NLTE – LTE) of  $+0.03$  dex.

[Korotin et al. \(2015\)](#) computed NLTE equivalent widths (EW) and NLTE abundance corrections for the four main Ba II lines: 4554.0, 5853.7, 6141.7, and 6496.9 Å. By comparing LTE and NLTE abundances, they showed that the LTE calculations for the weaker 5853.7 Å line tend to yield LTE abundances close to the NLTE ones, and that the difference between the LTE and NLTE abundance for the three red Ba lines is on average  $\pm 0.1$  dex. In some cases, the effect can reach 0.2 dex. They also showed that the 4554.03 Å line is not suitable for abundance determination.

More recently, NLTE departure coefficients for the large spectroscopic survey GALAH have been calculated by [Amarsi et al. \(2020\)](#) for 13 elements, including barium. They constructed grids of departure coefficients that have been implemented into the GALAH Data Release 3 analysis pipeline in order to complement the existing NLTE grid for iron. Their grids cover the range of metallicity and gravities encountered in our sample. They studied the Ba II lines at 5853.7 Å and 6496.9 Å and derived

an abundance correction (NLTE – LTE) ranging from  $-0.01$  to  $0.18$  dex.

We computed independent 3D NLTE corrections of the barium abundances based on 3D NLTE – 1D LTE grids recently computed by [Gallagher et al. \(in prep.\)](#). The tables representing the Ba abundance correction grids can be found online at [ChETEC-INFRA<sup>2</sup>](#), together with background information and instructions on how to use the corrections. The solar 3D NLTE barium abundance used for these correction grids ( $A(Ba)_{3D-NLTE}^{\odot} = 2.27$ ) was taken from [Gallagher et al. \(2020\)](#).

Unfortunately, most of our MINCE sample of stars have very low  $T_{\text{eff}}$  and  $\log g$  values that are not covered by the [Gallagher et al.](#) correction grid. In order to obtain corrections for at least a few targets, we chose to derive corrections using a nearest-neighbour interpolation approach; that is, we assumed  $\log g = 1.5$  for targets with gravities in the range  $1.0 < \log g \leq 1.5$ . Table 3 shows the 3D NLTE corrections (the Ba corr columns) for the three main Ba II lines. These corrections are to be added to the 1D LTE barium abundance,  $A(Ba)$ , to obtain the 3D NLTE Ba abundance ( $A(Ba)_{3D-NLTE} = \log(N(Ba)) - \log(N(H)) + 12$ ). The corrections for  $[Ba/H]$  or  $[Ba/Fe]$  are given by the difference of stellar minus solar corrections.

The results are plotted in Fig. 1. The blue dots represent the uncorrected 1D LTE  $[Ba/Fe]$  abundance of our sample stars. The green dots indicate the  $[Ba/Fe]$  abundances of the five targets listed in Table 3 after correction for 3D NLTE effects.

The final corrections for  $[Ba/Fe]$  are of the order of  $\approx 0.1$  dex over the range of metallicity in our sample. Importantly, the 3D NLTE corrections do not significantly affect the trend of  $[Ba/Fe]$  abundances with metallicity.

Europium NLTE corrections have been computed by [Mashonkina et al. \(2008\)](#) for HD 125563, a cool metal-poor giant ( $[Fe/H] \approx -2.6$  dex). They determined a NLTE – LTE abundance correction of 0.12 dex.

From these studies, we can conclude that NLTE effect corrections for barium and europium are rather small compared to the large range of abundance ratios of  $[Sr/Fe]$  and  $[Ba/Fe]$ . Moreover, it is unlikely that the dispersion found for these abundance ratios at a given metallicity can be attributed to the adopted LTE assumption.

#### 4.4. Error budget

Table 4 lists an estimate of the errors that are due to typical uncertainties in the stellar parameters. We adopted the uncertainties on the stellar parameters as:  $\Delta T_{\text{eff}} = 100$  K,  $\Delta \log g = 0.20$  dex, and  $\Delta \xi = 0.2$  km  $s^{-1}$ . These are typical uncertainties used to estimate the sensitivity of each parameter on the abundance determination. These adopted uncertainties for  $T_{\text{eff}}$  and  $\log g$  are of the order of the standard deviation found between the stellar parameters derived using MyGisFos ([Sbordone et al. 2014](#)) taken in [Cescutti et al. \(2022\)](#) and the stellar parameters obtained by Starhorse ([Anders et al. 2019](#)). More details can be found in [Cescutti et al. \(2022\)](#). The 0.2 km  $s^{-1}$  error on the microturbulence velocity corresponds to the acceptable variation of this parameter, giving abundances of Fe I independently of the excitation potential of the line. A change in the stellar parameters leads to a change in the  $[X/Fe]$  abundance derived for the star.

These errors were estimated by varying  $T_{\text{eff}}$ ,  $\log g$ , and  $\xi$  in the model atmosphere of BD +11 2896. We chose this star as the

<sup>2</sup> <http://chetec-infra.eu/3dnlte>

**Table 3.** Barium 3D NLTE corrections for a subset of stars, computed for the Ba II lines at 5853.7 Å, 6141.7 Å, and 6496.9 Å.

Star	$T_{\text{eff}}$	$\log g$	[Fe/H]	[Ba/Fe]	Ba corr	[Ba/Fe]	Ba corr	[Ba/Fe]	Ba corr	Eq. width 5853.7	Ba corr
				5853.7	5853.7	6141.7	6141.7	6496.9	6496.9		
Sun	5770	4.44	0.00	0.00	0.09	0.00	0.06	0.00	0.05	–	–
HD 115575	4393	1.50	-1.99	-0.32	0.17	-0.22	0.11	-0.21	0.10	83.0	0.2
BD +48 2167	4468	1.50	-2.29	-0.13	0.22	-0.03	0.12	0.02	0.11	83.5	0.2
BD +11 2896	4254	1.50	-1.41	0.02	0.03	0.12	-0.01	0.02	-0.06	120.8	0.067
BD -00 4538	4482	1.50	-1.90	-0.03	0.23	0.07	0.12	0.02	0.12	98.8	0.216
BD +03 4904	4497	1.50	-2.58	-0.31	0.18	-0.36	0.12	-0.41	0.14	49.2	0.177

**Notes.** Given the 1D LTE Ba abundance [Ba/Fe], they are extracted from the 3D NLTE – 1D LTE tables provided by Gallagher et al. (in prep). The last two columns give the measured EW of the barium line at 5853.7 Å and the corresponding barium abundance correction computed by a slightly different interpolation method from the same tables.

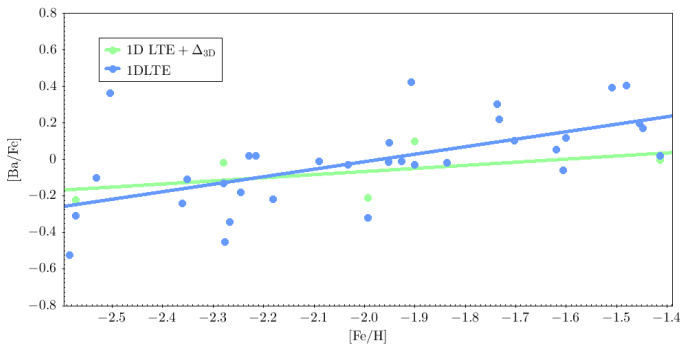


**Fig. 1.** Barium abundance, [Ba/Fe], versus metallicity, [Fe/H]. Blue dots represent the 1D LTE barium abundances derived from the barium line at 5853 Å. Green dots represent the corrected [Ba/Fe] values obtained for a subset of five stars by adding the 3D NLTE corrections ( $\text{Ba corr}^{(3D)} - \text{Ba corr}^{(1D)}$ ) given in Table 3 to the 1D LTE [Ba/Fe] abundance. The blue line (resp. green line) is the linear fit to the 1D LTE (3D NLTE) abundances.

determination of the abundances of all the elements analysed in the article was possible.

As the stars in our sample have stellar parameters close to BD +11 2896, the other stars yield similar results. In particular, this is also the case for the lower metallicity range of our sample of stars.

The total error was estimated by adding the quadratic sum of the uncertainties in the stellar parameters and the error in the fitting procedure of the synthetic spectrum and the observed spectrum (the main source of error comes from the uncertainty in the placement of the continuum). The error in the fitting procedure can be estimated by determining the line-to-line scatter of the abundance when several lines of a given element are available. These errors are given in Table A.3.

## 5. Results

In Table A.3, we present the results of the abundance determination. For each element, we give the [X/H] ratios and the  $\sigma(X)$ , calculated as the standard deviation of the mean value when abundance determination from several lines is given. [Fe I/H] and [Fe II/H] are from MINCE I. Hyphens in the table means that the corresponding line was severely blended and the blend was dominated by other lines, rendering an abundance determination impossible.

**Table 4.** Sensitivity of abundances on atmospheric parameters.

Element	$\Delta T_{\text{eff}}$	$\Delta \log g$	$\Delta \xi$
	+100 K	+0.2 dex	0.2 km s <sup>-1</sup>
Sr I	-0.05	-0.02	+0.05
Y II	-0.03	-0.12	+0.05
Zr II	+0.02	-0.15	+0.04
Ba II	-0.05	-0.11	+0.28
La II	-0.05	-0.12	+0.01
Ce II	-0.07	-0.11	+0.03
Pr II	-0.04	-0.12	+0.00
Nd II	-0.04	-0.13	+0.00
Sm II	-0.06	-0.12	+0.02
Eu II	-0.02	-0.12	+0.01

### 5.1. General comparison with literature results

In Figs. 2–4, we show our results, compared with data from a large compilation of results found in the SAGA database (Suda et al. 2008). In this compilation, all the abundance ratios [X/Fe] have been recalculated with the solar abundances of Asplund et al. (2009). We did not apply any abundance corrections to take into account the difference between the solar abundances adopted in our study and the ones used in the SAGA database data. For all the elements but one (Lanthanum), the difference ranges from 0.00 to 0.05. For La, our adopted solar abundance is 0.09 dex higher than in Asplund et al. (2009). We have also added (shown with black symbols) the abundance results from François et al. (2007), using the large programme “First Stars” sample (Cayrel et al. 2004). Although the “First Stars” sample is dedicated to extremely metal-poor stars, their abundances have been determined by the same methods (i.e., atomic data, synthesis code). The continuity in the abundance trends, [X/Fe] versus [Fe/H], is a good indicator that no systematic offset is present in the analysis of this sample of moderately metal-poor stars.

The comparison of our abundance ratios with the literature data does not show any offset or a different trend to [Fe/H] or [Ba/H]. The only significant difference is a visibly lower dispersion as a function of [Fe/H].

### 5.2. Comparison with main-sequence turn-off star abundances

The main goal of this comparison is to evaluate the possible offsets or trends that could appear from the use of a different set

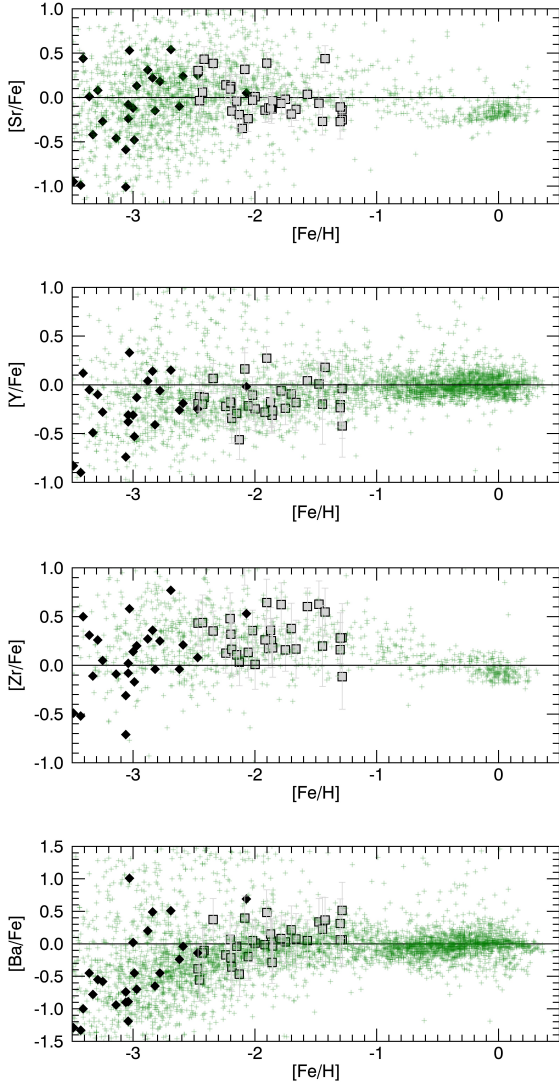


**Fig. 2.** Abundance ratios of  $[\text{Sr}/\text{Fe}]$ ,  $[\text{Y}/\text{Fe}]$ ,  $[\text{Zr}/\text{Fe}]$ , and  $[\text{Ba}/\text{Fe}]$  as a function of  $[\text{Fe}/\text{H}]$  for the stars of our sample, shown as grey squares. We added the stars from the SAGA database (Suda et al. 2008), which are represented by green crosses. Results for very metal-poor stars from François et al. (2007) are shown as black diamonds.

of absorption lines or the same lines with different strengths. As our sample is made of mildly metal-poor giant stars, the lines we measured are stronger than in dwarf stars. They can also be affected by more severe blends.

In Fig. 5, we plot the abundance ratios  $[\text{Sr}/\text{Fe}]$  and  $[\text{Ba}/\text{Fe}]$  as a function of  $[\text{Fe}/\text{H}]$  for our sample of stars. We have added the abundance results for a sample of main-sequence stars from Roederer et al. (2014) to see possible differences between evolved and un-evolved stars.

In our project, we have chosen to observe giant stars for two main reasons. The first is that they are intrinsically brighter and easier to observe with 2-meter-class telescopes. Even with telescopes with moderate apertures, we can obtain spectra for a large sample of giant stars with exposure times not exceeding 1 h. The second and most important reason is that we can detect more neutron-capture element species that can only be measured from weak lines not visible in the spectra of main-sequence turn-off stars. In Fig. 5, we highlight two important neutron-capture elements. These elements are crucial as some of their lines can be

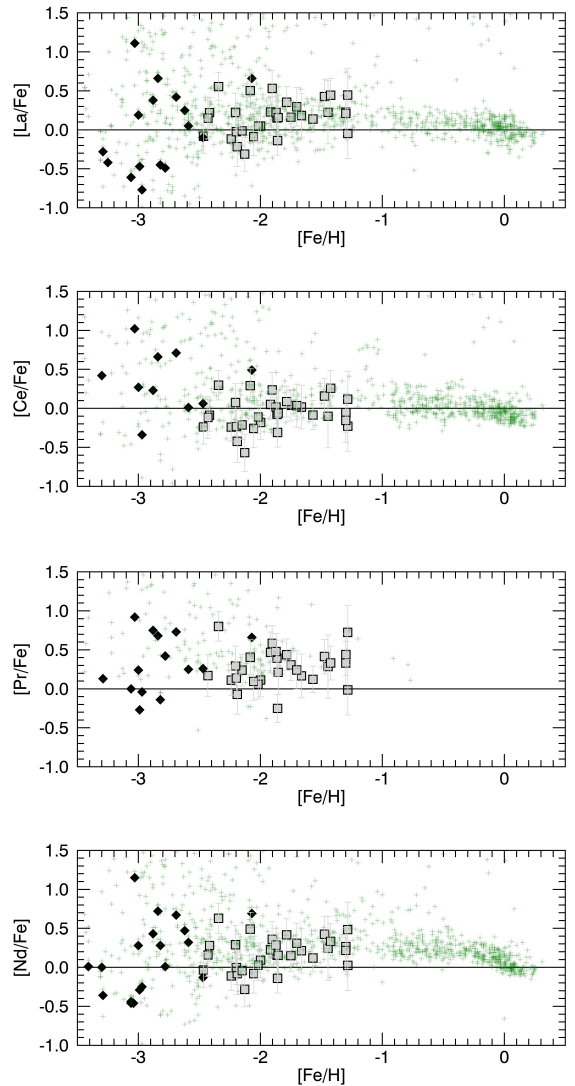


**Fig. 3.** Abundance ratios of  $[\text{La}/\text{Fe}]$ ,  $[\text{Ce}/\text{Fe}]$ ,  $[\text{Pr}/\text{Fe}]$ , and  $[\text{Nd}/\text{Fe}]$  as a function of  $[\text{Fe}/\text{H}]$  for the stars in our sample shown as grey squares. We added the stars from the SAGA database (Suda et al. 2008), which are represented by green crosses. Results for very metal-poor stars from François et al. (2007) are shown as black diamonds.

detected in the most metal-poor stars. Our figures show that no difference is found in the location of the abundance trends of  $[\text{Sr}/\text{Fe}]$  and  $[\text{Ba}/\text{Fe}]$  versus  $[\text{Fe}/\text{H}]$ . However, we note that the results for main-sequence stars show a smaller dispersion.

### 5.3. Galactic substructures

Recent years have witnessed significant strides in our understanding of the accretion history of the Milky Way. Thanks to *Gaia* kinematics results, it is now possible to identify stars in the solar vicinity that may be the result of past accretion events (see e.g. Helmi 2020, and references therein). One should however keep in mind that even a single accretion event may result in multiple dynamical substructures (Jean-Baptiste et al. 2017) and that a purely dynamical selection is always subject to contamination (see e.g. the discussion on the metallicity distribution function of GSE in Bonifacio et al. 2021); hence, the interest in complementing the dynamical information with chemical information. Concurrently, advancements in the theoretical framework have

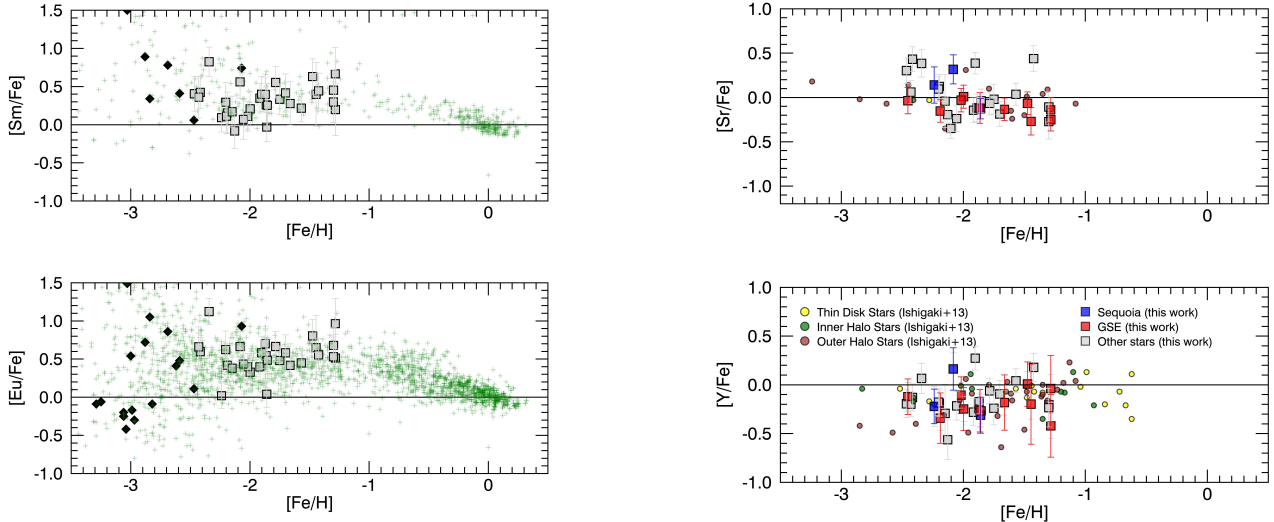


**Fig. 4.** Abundance ratios of  $[\text{Sm}/\text{Fe}]$  and  $[\text{Eu}/\text{Fe}]$  as a function of  $[\text{Fe}/\text{H}]$  for the stars in our sample shown as grey squares. We added the stars from the SAGA database, which are represented by green crosses. Results for very metal-poor stars from François et al. (2007) are shown as black diamonds.

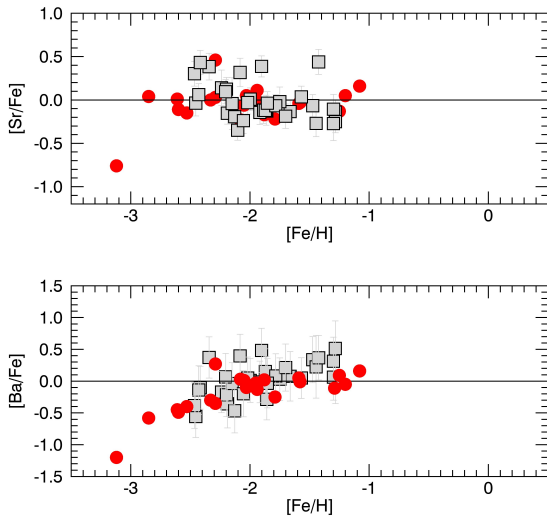


**Fig. 5.** Abundance ratios of  $[\text{Sr}/\text{Fe}]$  and  $[\text{Ba}/\text{Fe}]$  as a function of  $[\text{Fe}/\text{H}]$ . Our sample is represented as grey squares. Main-sequence stars from Roederer et al. (2014) are shown as red circles.

paralleled these observations, enhancing our comprehensive understanding of the complex processes governing the Milky Way’s accretion history (Calura & Menci 2009; Murphy et al. 2022; García-Bethencourt et al. 2023). In MINCE I, kinematics and action properties have been used to identify several stars likely belonging to the GSE (Belokurov et al. 2018; Haywood et al. 2018; Helmi et al. 2018) and Sequoia (Barbá et al. 2019; Villanova et al. 2019; Myeong et al. 2019) accretion events. In this section, we present our results and compare them with literature data, taking into account the substructure with which the stars can be associated. For our sample of stars, we adopted the separation into GSE, Sequoia, and thin or thick discs, as was suggested by MINCE I. The stars not identified in these three categories are halo stars. In this sample, TYC 3085-119-1 was considered to be a thick-disc star, following the classification of Bensby et al. (2014).

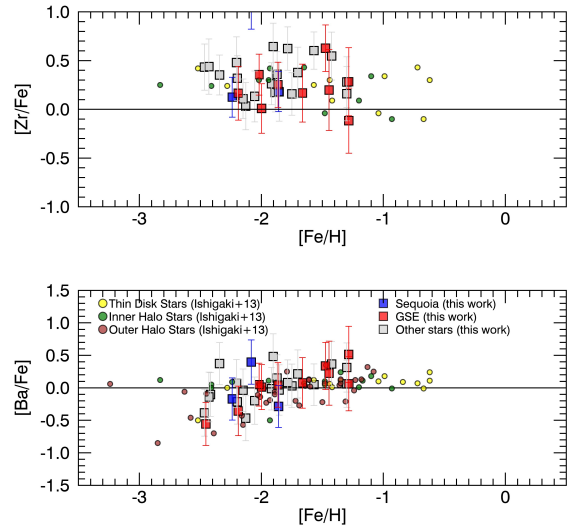


**Fig. 6.** Abundance ratios of  $[\text{Sr}/\text{Fe}]$ ,  $[\text{Y}/\text{Fe}]$ ,  $[\text{Zr}/\text{Fe}]$ , and  $[\text{Ba}/\text{Fe}]$  as a function of  $[\text{Fe}/\text{H}]$  for the stars in our sample shown as square symbols. Red squares represent stars from GSE, while blue squares are stars identified as Sequoia stars. Grey squares are the remaining halo stars. We added the stars Ishigaki et al. (2013), which are represented as circles: respectively, disc stars in yellow, inner halo stars in green, and outer halo stars in brown.

Among the large set of results that can be found in the literature, we selected a sample where the separation between galactic components (thick disc, inner halo, and outer halo) was considered. The paper from Ishigaki et al. (2013) gathers a good sample of stars from the different sub-components of the Galaxy.

The results are presented in Figs. 6, 7 and 8. Our stars are shown as grey squares. Blue squares represent stars from GSE and red squares are stars identified as Sequoia stars. Grey squares are the remaining stars, mostly halo stars. The results from Ishigaki et al. (2013) are divided into outer halo stars (brown circles), inner halo stars (green circles), and thick-disc stars (yellow circles).

It is interesting to note that for most of the elements, the  $[\text{X}/\text{Fe}]$  versus  $[\text{Fe}/\text{H}]$  found for the GSE stars seems to follow a rather well-defined trend, with a much smaller dispersion than that of the remaining sample of halo stars. For the Sequoia stars, it is not possible to conclude anything about a peculiar behaviour

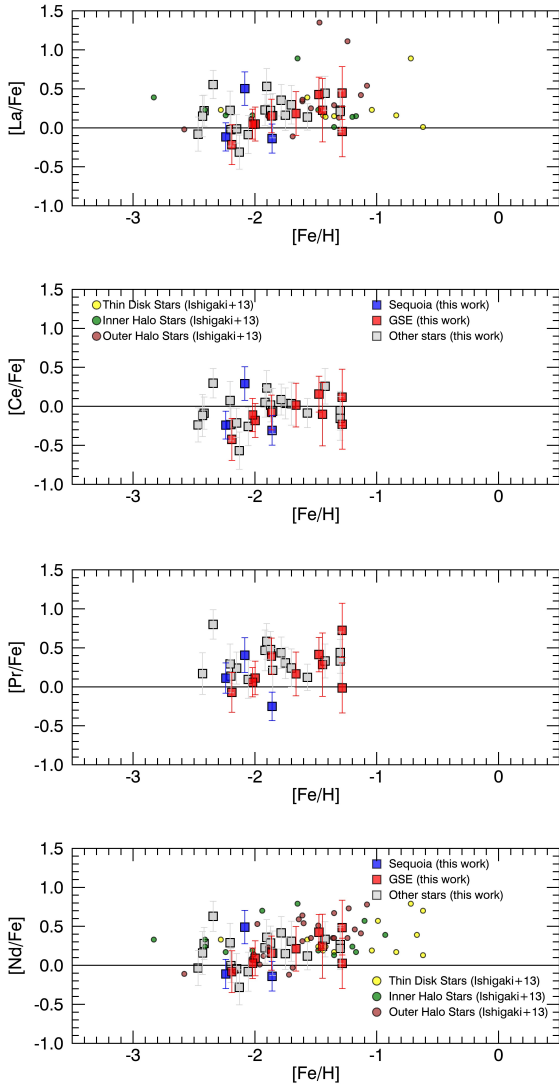


**Fig. 7.** Abundance ratios of [La/Fe], [Ce/Fe], [Pr/Fe], and [Nd/Fe] as a function of [Fe/H] for the stars in our sample shown as square symbols. We added the stars from Ishigaki et al. (2013), which are represented as circles: respectively, disc stars in yellow, inner halo stars in green, and outer halo stars in brown.

of the [X/Fe] versus [Fe/H] distribution. Our results are in agreement with the abundance ratios found by Ishigaki et al. (2013) for the outer and inner halo stars.

#### 5.4. Neutron-capture element abundance ratios

In Fig. 9, we plotted the abundances ratios [Sr/Ba] and [Eu/Ba] as a function of [Fe/H] and [Ba/H] for our sample of stars. We added the results from Ishigaki et al. (2013). The symbols are the same as in Fig. 6.

The [Eu/Ba] is representative of the relative production of the r-process relative to the s-process in these metal-poor stars. The results show the well-known constant ratio [Eu/Ba] with a level of  $\approx +0.6$  dex, which is slightly lower than the pure r-component value of  $\approx +0.7$  dex computed by Arlandini et al. (1999). It is interesting to note that the median value found for the GSE sample is larger ( $\langle [Eu/Ba] \rangle = 0.45$  dex) than the one found for the Sequoia stars ( $\langle [Eu/Ba] \rangle = 0.27$  dex), indicating a different level of enrichment of the matter that formed these two systems.

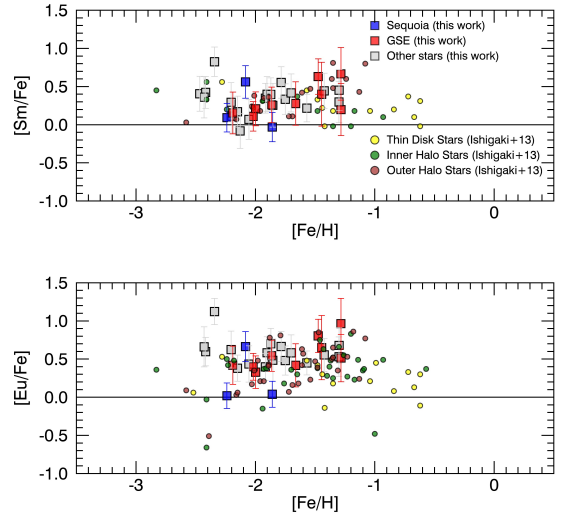


**Fig. 8.** Abundance ratios of [Sm/Fe] and [Eu/Fe] as a function of [Fe/H] for the stars in our sample shown as square symbols. We added the stars from Ishigaki et al. (2013), which are represented as circles: respectively, disc stars in yellow, inner halo stars in green, and outer halo stars in brown.

This difference will be studied in light of the models of galactic chemical evolution in Sect. 7.

The [Sr/Ba] versus [Fe/H] and [Sr/Ba] versus [Ba/H] are particularly interesting. From the top, the second panel of Fig. 9 shows the variation in [Sr/Ba] as a function of [Ba/H]. The results for the GSE stars show a tight relation between [Sr/Ba] and [Ba/H], with a regression coefficient of  $-0.94$ . This result, which needs to be confirmed with a larger sample, shows how the chemical enrichment of the GSE has evolved over a range of 2 dex in [Ba/H]. The Sequoia stars follow the same trend; that is, a decreasing [Sr/Ba] as [Ba/H] increases, with a slight difference. Indeed, at a given [Ba/H], the [Sr/Ba] ratio found in the Sequoia stars seems higher than the value found in GSE stars. This difference in Galactic chemical evolution of these two components will be addressed in Sect. 7.

## 6. GSE and Sequoia substructures

The aim of this section is to compare our results for the stars belonging to GSE and Sequoia with existing literature results based on high-resolution spectroscopy. Until now, there have only been a handful of papers in which detailed neutron-capture abundances have been computed. Spectroscopic surveys have been used to characterise the chemical properties of halo substructures. In general, these studies concentrate on a small number of elements and mostly light metals (e.g. Hasselquist et al. 2021; Buder et al. 2022). A more extended analysis of a larger number of elements (13 elements) has been made by Horta et al. (2023) using APOGEE data. Unfortunately, this study contains only cerium as a neutron-capture element. A few studies based on follow-up programs of smaller samples using high-resolution spectrographs have included some neutron-capture elements in their analysis. Limberg et al. (2021) has analysed a sample of stars belonging to the Helmi stream and derived Eu and Ba abundances for a couple of stars in their sample. Aguado et al. (2021) derived the abundances of Sr, Ba, and Eu in a sample of GSE and Sequoia stars. Matsuno et al. (2022) studied a sample of stars belonging to Sequoia and determined the abundances of several elements, among them Sr and Y.

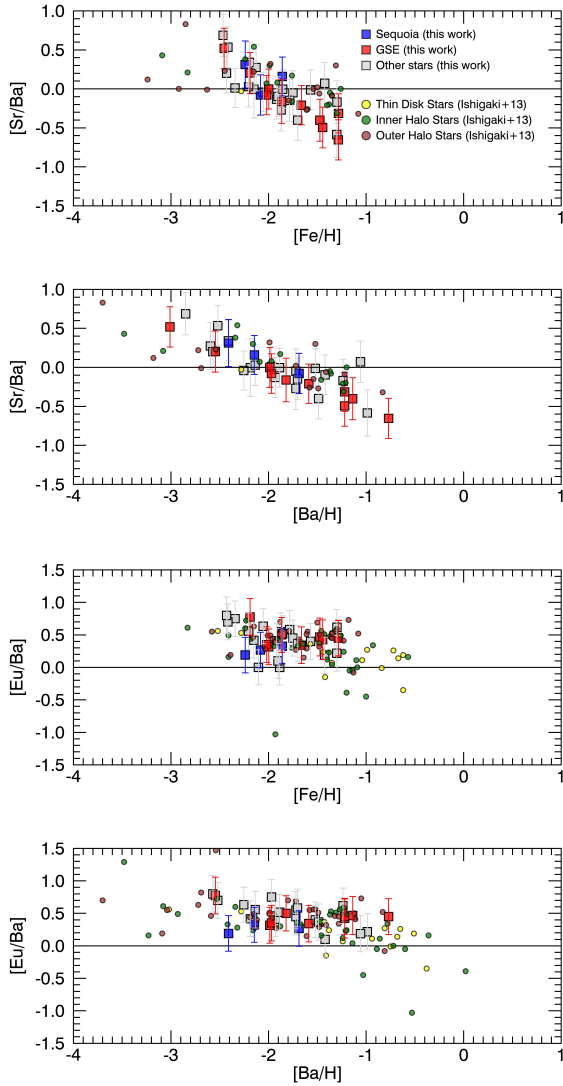


**Fig. 9.** Abundance ratios of  $[Sr/Ba]$  and  $[Eu/Ba]$  as a function of  $[Fe/H]$  (panels one and three) and as a function of  $[Ba/H]$  (panels two and four) for the stars in our sample, shown as square symbols. We added the stars from Ishigaki et al. (2013), represented as circles.

Figure 10 represents  $[Y/Fe]$  and  $[Y/Ba]$  as a function of  $[Fe/H]$  and  $[Ba/H]$  for our sample of stars. The stars are shown as square symbols with the same colour scheme as in Fig. 9. We have added the results for the Sequoia stars analysed by Matsuno et al. (2022). We find results compatible with a constant  $[Y/Fe]$ , although with a significant dispersion, over a range of metallicities from  $[Fe/H] \approx -2.4$  dex to  $[Fe/H] \approx -1.2$  dex if both samples are combined. For the  $[Ba/Fe]$  versus  $[Fe/H]$ , the trend could also be interpreted as a constant value with a large dispersion, with a mean value of around  $-0.2$  dex. The  $[Y/Ba]$  ratio gives very different results. The values found by Matsuno et al. (2022) appear to be significantly higher than our results.

In Fig. 11, we plot the  $[Sr/Ba]$  and  $[Eu/Ba]$  ratios as a function of  $[Fe/H]$  and  $[Ba/H]$  for our sample of stars. We have added the results for the GSE stars analysed by Aguado et al. (2021). We do not confirm the high  $[Eu/Ba]$  that they found in their sample. It is interesting to note that the  $[Eu/Ba]$  ratio found by François et al. (2007) was not as high as that found in the stars of Aguado et al. (2021). Concerning the  $[Sr/Ba]$  ratio versus  $[Fe/H]$ ,

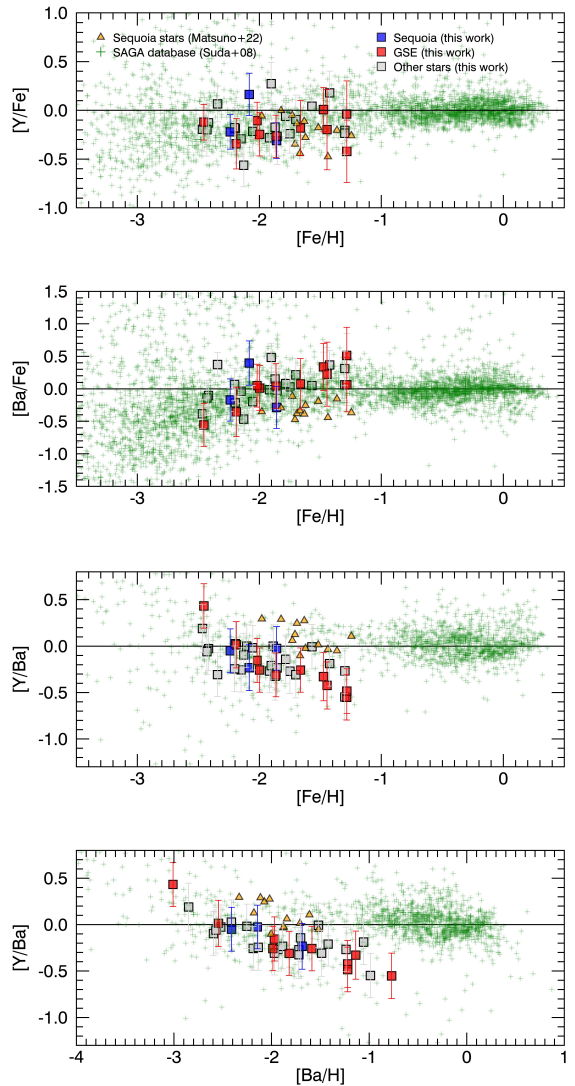


**Fig. 10.** Abundance ratios of  $[Y/Fe]$  and  $[Ba/Fe]$  as a function of  $[Fe/H]$  for the stars in our sample as square symbols. Matsuno et al. (2022) results for Sequoia stars have been added and shown as orange triangles. Green symbols represent stars from the SAGA database (Suda et al. 2008).

we found ratios in reasonable agreement with their values. However, our results seem to indicate a tight relation between the  $[Sr/Ba]$  and  $[Fe/H]$  ratio, whereas they found a ratio compatible with a constant value of  $\approx -0.30$  dex and with a dispersion of  $\approx 0.20$  dex.

This first limited sample of the MINCE project does not allow us to draw firm conclusions about the characteristic abundances of the well-identified galactic sub-components of our Galaxy, but clearly shows the potential of the study of neutron-capture elements in intermediate-metallicity stars. Analysis of a larger sample is needed to understand these differences better.

## 7. Reference chemical evolution models

One of the more striking features of the results obtained for the abundances of neutron-capture elements is the strong correlation of the data for GSE in the  $[Sr/Ba]$  versus  $[Ba/H]$  plane. With this first sample of MINCE stars, our aim is to investigate this feature by means of a stochastic chemical evolution model, based on the

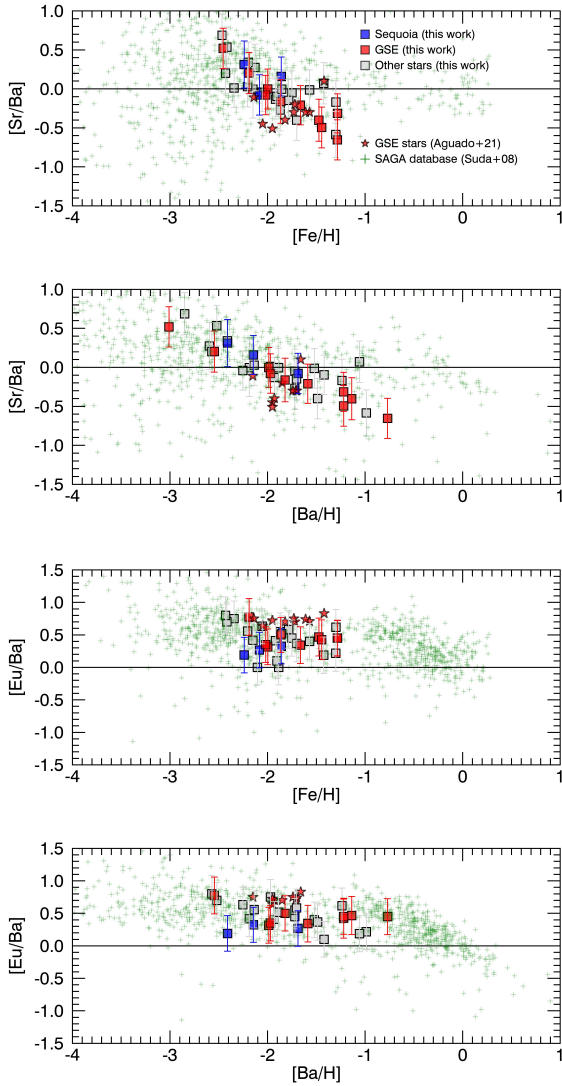


**Fig. 11.** Abundance ratios of  $[Y/Fe]$  and  $[Ba/Fe]$  as a function of  $[Fe/H]$  for the stars in our sample are shown as square symbols. [Aguado et al. \(2021\)](#) results for GSE stars have been added and shown as red stars. Green symbols represent halo stars from the SAGA database ([Suda et al. 2008](#)).

original code developed in [Cescutti \(2008\)](#). In this work, we try to reproduce the evolution of GSE and we use the same parameters as in the chemical evolution model used in [MINCE I](#), but within a stochastic framework. GSE chemical evolution parameters were tuned to match the metallicity distribution function of GSE stars described in [Cescutti et al. \(2020\)](#). Overall, its evolution is similar to that of a dwarf galaxy with a mass of about 3% of the Milky Way; however, given its galactic winds and an inefficient star formation ending more than 5 Gyr ago, its stellar content is only around 1% of the Galactic one. These results are similar to the ones obtained for the chemical evolution of GSE in [Vincenzo et al. \(2019\)](#). In the stochastic model, we have to consider a typical volume in which the gas is always well mixed. For this model, the fixed volume has a radius of 150 pc and a total infalling mass of  $2.6 \cdot 10^5 M_{\odot}$ . The nucleosynthesis considered is the same as in [Cescutti & Chiappini \(2014\)](#), so we take into account these prescriptions for the neutron-capture elements: the r-process enrichment from magneto-rotational-driven supernovae (SNe; [Winteler et al. 2012](#); [Nishimura et al.](#)

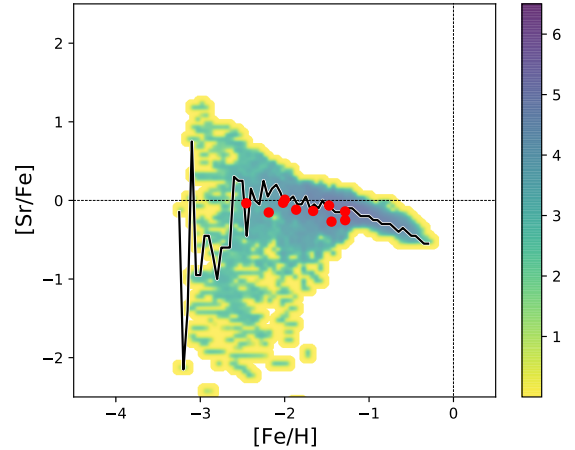


**Fig. 12.** Abundance ratios of  $[Sr/Fe]$  versus  $[Fe/H]$ . The red dots are the abundances of the GSE stars in our sample; the colour-coded area shows the results of the stochastic model. The colour coding is described in the bar as the number density of long-living stars in log-scale. The black line shows the most probable value of the model in  $[Sr/Fe]$  at each bin in  $[Fe/H]$ .

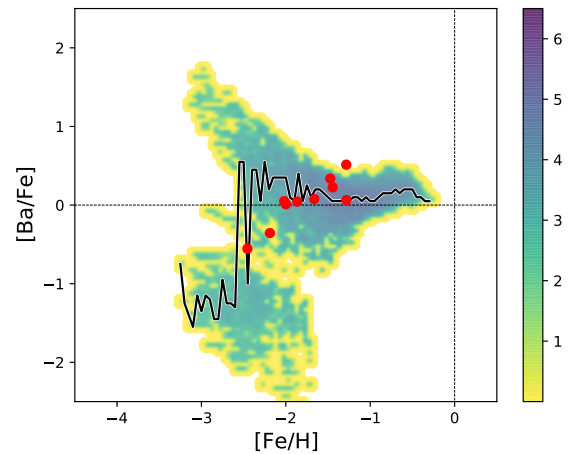


**Fig. 13.** Same as Fig. 12, but for the abundance ratios of  $[Ba/Fe]$  versus  $[Fe/H]$ .

2015); the s-process production from asymptotic giant branch (AGB) stars described in [Cristallo et al. \(2009, 2011\)](#); and the s-process production from rotating massive stars taken from [Frischknecht et al. \(2012, 2016\)](#). It is worth underlining that the use of the yields of [Limongi & Chieffi \(2018\)](#), although with different velocities, would not alter the results ([Prantzos et al. 2018](#); [Rizzuti et al. 2019, 2021](#)). Similarly, considering neutron star mergers under specific characteristics that allow them an almost prompt enrichment of the Galaxy produces results similar to magneto-rotational-driven SNe ([Cescutti et al. 2015](#); [Cavallo et al. 2021, 2023](#)). Iron is produced both by massive stars, with a fixed production assumed to be  $0.07 M_{\odot}$  (see [Limongi & Chieffi 2018](#)) and SNe Ia, with the classic delay time adopted by [Matteucci & Greggio \(1986\)](#) and the [Iwamoto et al. \(1999\)](#) yields.

### 7.1. Results of $[Sr/Fe]$ , $[Ba/Fe]$ and $[Eu/Fe]$ versus $[Fe/H]$ for the Gaia Sausage Enceladus galaxy

In Figs. 12, 13, and 14, we present the comparison between the model results and the abundances measured for GSE. Small

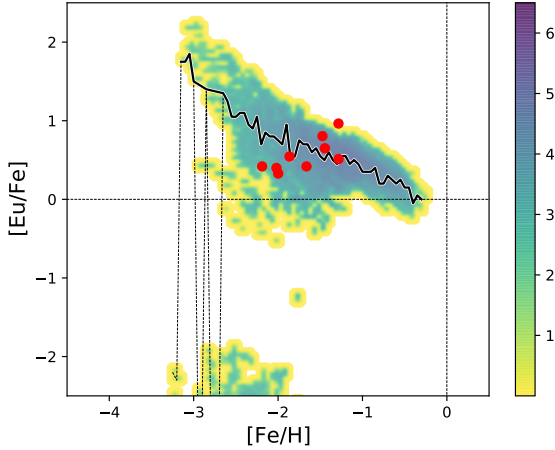


**Fig. 14.** Same as Fig. 13, but for the abundance ratios of [Eu/Fe] versus [Fe/H]. The black line shows the most probable value of the model in [Eu/Fe] at each bin in [Fe/H]. We exclude the abundances with [Eu/Fe] < -2, since these extremely low abundances in europium are hardly measurable. The line obtained including these extreme values is displayed with a tiny dashed line.

adjustments were applied to reproduce at best the data for barium and strontium; the model results for barium were modified by +0.2 dex and strontium by -0.1 dex. These adjustments are probably due to our assumptions about nucleosynthesis; for example, they can be explained by a more efficient production of barium in rotating massive stars or a more complex production by the r-process events. In any case, these elements are mostly produced by the s-process in AGB stars at solar metallicity, so these tiny adjustments would not significantly vary the predictions for the solar abundances. Another possibility is that the 1D LTE chemical abundances are affected by offsets not considered due to NLTE and/or 3D corrections.

The abundances of [Sr/Fe] versus [Fe/H] of the GSE stars are all well explained by the model results in Fig. 12; they are also located well within the boundaries of the colour distribution, in the region of the [Sr/Fe] versus [Fe/H] plane where we expect the larger fractions of GSE. We also note a severe decrease in the dispersion at [Fe/H]  $\geq$  -1.2. More data will be useful in this area; that is, slightly above the metallicity considered by MINCE stars. We also see that the dispersion of our sample seems quite reduced for the stars in our sample. The stochastic volumes considered may be too small for this system; given the amount of data collected, we prefer to keep this parameter fixed. We also present in each plot a line connecting the most likely value obtained by the model at each metallicity (either in [Fe/H] or [Ba/H]). The purpose of this line is to provide the most likely observed abundances, and it is clear that overall the model is closely following the abundances measured in the MINCE sample. For barium in Fig. 13 and europium in Fig. 14, the comparisons between measured abundances and model results are similar. The small cloud of the model results, showing a very low europium abundance ([Eu/Fe] < -2), is due to the tiny amount of europium produced by the rotating massive stars and corresponds to the cloud presented by barium in the range  $-2.5 \geq$  [Ba/Fe]  $\geq$  -1.0. Most of the data points are well inside the model predictions; we do not find any stars sitting in the r-process rich star locus – the tail at high [Eu/Fe] (or [Ba/Fe]) at [Fe/H]  $\sim$  -2.5. This is expected given the rarity of these objects, the small sample for GSE, and considering also that, by construction, the MINCE sample does not include

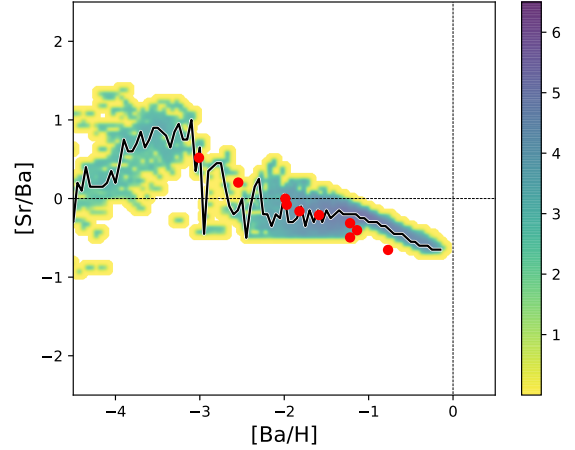


**Fig. 15.** Abundance ratios of [Sr/Ba] versus [Ba/H]. The red dots are the abundances of the GSE stars in our sample; the colour-coded area shows the results of the stochastic model. The colour coding is described in the colour bar as the number density of long-lived stars on a log-scale.

extremely metal-poor stars. We have one star in the MINCE sample that is actually in this zone (BD +21 4759), but it is not shown here since it does not belong to GSE. Nonetheless, we also note that we have an outlier (BD -04 18); this star is just at the border of the models and is (practically) a europium-rich star, with [Eu II/Fe I]=1.16 and [Eu II/Fe II]=0.96. We cannot easily explain this, but we note that the [Ba/Eu] ratio of this star is close to the pure r-process ratio and that it is actually the star with the highest abundance of both barium and europium, given also that it is one of the most metal-rich within the sample. Could this be the signature of an extremely high enrichment by a delayed source of the r-process (a neutron star merger)? Clearly, a single system is not enough to support this claim; still, it is a rather peculiar object in terms of barium and europium enrichment, and we will search for more of these objects in future MINCE works.

## 7.2. Results for [Sr/Ba] and [Eu/Ba] versus [Ba/H]

In Fig. 15, we present the model and the stellar abundance results for GSE in the [Sr/Ba] versus [Ba/H] plane. As was mentioned previously, the results of the stellar abundances are striking, as they show a distinct correlation between strontium and barium in this plane; similar to the [Ba/Fe] versus [Fe/H] case, the model reproduces fairly well most of the data, except the most barium-rich star of the sample BD+04 18. It should be added that the dispersion of the model does not predict the observed correlation; on the other hand, the most probable stellar abundances predicted by the model are close to the observational trend. In this plot, the area with [Ba/H] < -3 is enriched only by the rotating massive stars, with a low barium enrichment and a dispersion between [Sr/Ba] depending on the mass of the stars. The dispersion at  $-2.5 <$  [Ba/H] < -1.5 is created mostly by the pollution of the r-process events, but there is also a mild contribution coming from the rotating massive stars that produces the smaller variation in the [Sr/Ba] ratio. If we remove the s-process contribution from rotating massive stars and consider only r-process enrichment, our model will produce a constant [Sr/Ba] ratio. Therefore, to reproduce this observed correlation in [Sr/Ba], rotating massive stars represent a key ingredient. A possibility, not considered at the moment, is that the r-process production is more complex and there is an interplay between strontium and barium.

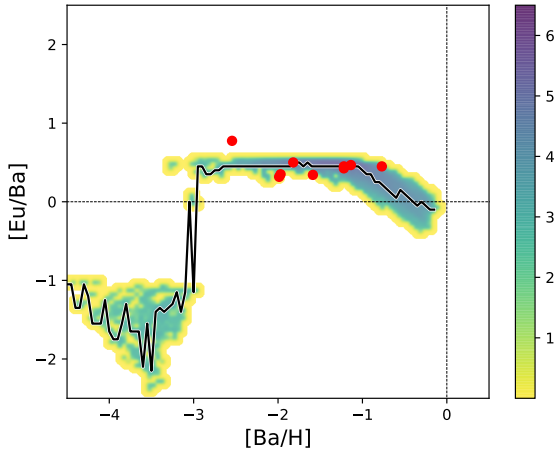


**Fig. 16.** Same as Fig. 15, but for the abundance ratios of [Eu/Ba] versus [Ba/H].

Finally, the region at  $[Ba/H] > -1$  is determined by the enrichment from AGB stars, which at low metallicities tend to produce a low  $[Sr/Ba]$  ratio.

Figure 16 shows that in the plane  $[Eu/Ba]$  versus  $[Ba/H]$  all of the stars are located on a narrow plateau associated with the assumed r-process production. We recall that the model assumes a variation in the barium of 0.2 dex, as was mentioned above; otherwise, the pure r-process would produce a ratio of  $[Eu/Ba]=0.7$  dex. In this plane, the only star that does not sit within the model prediction is TYC 4221-640-1. We also underline again that the enrichment by rotating massive stars produces the small spread in the model results in the range  $-2.5 < [Ba/H] < -1.5$ . The spread is smaller than the one in  $[Sr/Ba]$  because the theoretical predictions of barium enrichment of this source are quite small compared to those of strontium; according to the model, the region with  $[Eu/Ba] < -1$  is free from r-process pollution. In the abundance region  $[Ba/H] \leq -3$ , we will eventually find the (almost) Eu-free stars mentioned in Cescutti et al. (2015); Cavallo et al. (2021). Finally, the region at  $[Ba/H] > -1$  is created by the enrichment of AGB stars, producing a decreasing trend.

Overall, the model can explain the behavior found in the sample of GSE stars, but certainly further measurements are needed to strengthen these results or to disprove them.

## 8. Conclusions

This article is a follow-up on the work of MINCE I, which described the method adopted in the MINCE project to select the sample, determine the stellar atmosphere, and measure at intermediate-low metallicities the chemical abundances of several  $\alpha$  elements and iron peak elements, for a first sample of stars.

- We could determine the abundances for up to ten neutron-capture elements (Sr, Y, Zr, Ba, La, Ce, Pr, Nd, Sm, and Eu) in 33 stars. The general trends of  $[n\text{-capture element}/Fe]$  versus  $[Fe/H]$  abundance ratios are in agreement with the results found in the literature.
- When our sample is divided into galactic sub-components depending on their kinematics identified in MINCE I, we find that the variation in the  $[Sr/Ba]$  versus  $[Ba/H]$  ratio for the stars belonging to the GSE accretion event shows a tight anti-correlation.

- The results for the Sequoia stars, although based on a very limited sample, shows a  $[Sr/Ba]$  systematically higher than the  $[Sr/Ba]$  found for the GSE stars at a given  $[Ba/H]$ , hinting at a different chemical history. The variations in the  $[n\text{-capture}/Fe]$  abundance ratios for GSE, Sequoia, and the rest of the sample as a function of  $[Fe/H]$  do not show any systematic differences.
- Stochastic chemical evolution models were computed in order to help us understand the evolution of the GSE chemical composition of Sr and Ba with these characteristics: the same chemical evolution parameters of Cescutti et al. (2020), so compatible to those of a satellite galaxy with an original mass of 3% of the Milky Way, with an inefficient star formation ending more than 5 Gyr ago, and a stellar content that is around 1% of the Galactic stellar mass; the same nucleosynthesis for Sr and Ba considered in Cescutti & Chiappini (2014), so an r-process enrichment from magneto-rotational-driven SNe (Winteler et al. 2012) and an s-process production from AGB stars described in Cristallo et al. (2011); and an s-process production from rotating massive stars taken from Frischknecht et al. (2016). The preliminary conclusions are that this stochastic chemical evolution model’s predictions for Sr and Ba are compatible with this first sample of MINCE stars.

*Acknowledgements.* We gratefully acknowledge support from the French National Research Agency (ANR) funded project “Pristine” (ANR-18-CE31-0017). This work has made use of data from the European Space Agency (ESA) mission *Gaia* (<https://www.cosmos.esa.int/gaia>) to processed by the *Gaia* Data Processing and Analysis Consortium (DPAC, <https://www.cosmos.esa.int/web/gaia/dpac/consortium>). Funding for the DPAC has been provided by national institutions, in particular the institutions participating in the *Gaia* Multilateral Agreement. This work was also partially supported by the European Union (ChETEC-INFRA, project no. 101008324) This research has made use of the SIMBAD database, operated at CDS, Strasbourg, France. E.S. received funding from the European Union’s Horizon 2020 research and innovation program under SPACE-H2020 grant agreement number 101004214 (EXPLORE project). G.C. and L.M. acknowledge the grant PRIN project no. 2022X4TM3H “Cosmic POT” from Ministero dell’Università e la Ricerca (MUR). Funding for the Stellar Astrophysics Centre is provided by The Danish National Research Foundation (Grant agreement no.: DNRF106). We also acknowledge support from the CRC ELEMENTS.

## References

- Aguado, D. S., Belokurov, V., Myeong, G. C., et al. 2021, *ApJ*, 908, L8
- Alvarez, R., & Plez, B. 1998, *A&A*, 330, 1109
- Amarsi, A. M., Lind, K., Osorio, Y., et al. 2020, *A&A*, 642, A62
- Anders, F., Khalatyan, A., Chiappini, C., et al. 2019, *A&A*, 628, A94
- Arlandini, C., Käppeler, F., Wisshak, K., et al. 1999, *ApJ*, 525, 886
- Asplund, M., Grevesse, N., Sauval, A. J., & Scott, P. 2009, *ARA&A*, 47, 481
- Barbá, R. H., Minniti, D., Geisler, D., et al. 2019, *ApJ*, 870, L24
- Belokurov, V., Erkal, D., Evans, N. W., Koposov, S. E., & Deason, A. J. 2018, *MNRAS*, 478, 611
- Bensby, T., Feltzing, S., & Oey, M. S. 2014, *A&A*, 562, A71
- Bonifacio, P., Monaco, L., Salvadori, S., et al. 2021, *A&A*, 651, A79
- Bouchy, F., & Sophie Team. 2006, in *Tenth Anniversary of 51 Peg-b: Status of and prospects for hot Jupiter studies*, eds. L. Arnold, F. Bouchy, & C. Moutou, 319
- Buder, S., Lind, K., Ness, M. K., et al. 2022, *MNRAS*, 510, 2407
- Calura, F., & Menci, N. 2009, *MNRAS*, 400, 1347
- Cavallo, L., Cescutti, G., & Matteucci, F. 2021, *MNRAS*, 503, 1
- Cavallo, L., Cescutti, G., & Matteucci, F. 2023, *A&A*, 674, A130
- Cayrel, R., Depagne, E., Spite, M., et al. 2004, *A&A*, 416, 1117
- Cescutti, G. 2008, *A&A*, 481, 691
- Cescutti, G., & Chiappini, C. 2014, *A&A*, 565, A51
- Cescutti, G., Matteucci, F., Lanfranchi, G. A., & McWilliam, A. 2008, *A&A*, 491, 401
- Cescutti, G., Romano, D., Matteucci, F., Chiappini, C., & Hirschi, R. 2015, *A&A*, 577, A139
- Cescutti, G., Molaro, P., & Fu, X. 2020, *Mem. Soc. Astron. Italiana*, 91, 153
- Cescutti, G., Bonifacio, P., Caffau, E., et al. 2022, *A&A*, 668, A168

- Cosentino, R., Lovis, C., Pepe, F., et al. 2012, *SPIE Conf. Ser.*, **8446**, 84461V
- Cristallo, S., Straniero, O., Gallino, R., et al. 2009, *ApJ*, **696**, 797
- Cristallo, S., Piersanti, L., Straniero, O., et al. 2011, *ApJS*, **197**, 17
- Den Hartog, E. A., Lawler, J. E., Sneden, C., & Cowan, J. J. 2003, *ApJS*, **148**, 543
- Donati, J. F., Catala, C., Landstreet, J. D., & Petit, P. 2006, in *Solar Polarization 4*, eds. R. Casini, & B. W. Lites, *ASP Conf. Ser.*, **358**, 362
- Edvardsson, B., Andersen, J., Gustafsson, B., et al. 1993, *A&A*, **275**, 101
- Feuillet, D. K., Sahlholdt, C. L., Feltzing, S., & Casagrande, L. 2021, *MNRAS*, **508**, 1489
- François, P., Depagne, E., Hill, V., et al. 2007, *A&A*, **476**, 935
- Frischknecht, U., Hirschi, R., & Thielemann, F.-K. 2012, *A&A*, **538**, A2
- Frischknecht, U., Hirschi, R., Pignatari, M., et al. 2016, *MNRAS*, **456**, 1803
- Gaia Collaboration (Prusti, T., et al.) 2016, *A&A*, **595**, A1
- Gaia Collaboration (Brown, A. G. A., et al.) 2021, *A&A*, **649**, A1
- Gallagher, A. J., Bergemann, M., Collet, R., et al. 2020, *A&A*, **634**, A55
- García-Bethencourt, G., Brook, C. B., Grand, R. J. J., & Kawata, D. 2023, *MNRAS*, **526**, 1190
- Grevesse, N., & Sauval, A. J. 2000, in *Origin of Elements in the Solar System, Implications of Post-1957 Observations*, ed. O. Manuel, 261
- Gustafsson, B., Bell, R. A., Eriksson, K., & Nordlund, A. 1975, *A&A*, **42**, 407
- Gustafsson, B., Edvardsson, B., Eriksson, K., et al. 2003, in *Stellar Atmosphere Modeling*, eds. I. Hubeny, D. Mihalas, & K. Werner, *ASP Conf. Ser.*, **288**, 331
- Gustafsson, B., Edvardsson, B., Eriksson, K., et al. 2008, *A&A*, **486**, 951
- Hannaford, P., Lowe, R. M., Grevesse, N., Biémont, E., & Whaling, W. 1982, *ApJ*, **261**, 736
- Hansen, C. J., Bergemann, M., Cescutti, G., et al. 2013, *A&A*, **551**, A57
- Hasselquist, S., Hayes, C. R., Lian, J., et al. 2021, *ApJ*, **923**, 172
- Haywood, M., Di Matteo, P., Lehnert, M. D., et al. 2018, *ApJ*, **863**, 113
- Helmi, A. 2020, *ARA&A*, **58**, 205
- Helmi, A., Babusiaux, C., Koppelman, H. H., et al. 2018, *Nature*, **563**, 85
- Horta, D., Schiavon, R. P., Mackereth, J. T., et al. 2023, *MNRAS*, **520**, 5671
- Ishigaki, M. N., Aoki, W., & Chiba, M. 2013, *ApJ*, **771**, 67
- Ivans, I. I., Simmerer, J., Sneden, C., et al. 2006, *ApJ*, **645**, 613
- Ivarsson, S., Litzén, U., & Wahlgren, G. M. 2001, *Phys. Scr.*, **64**, 455
- Iwamoto, K., Brachwitz, F., Nomoto, K., et al. 1999, *ApJS*, **125**, 439
- Jean-Baptiste, I., Di Matteo, P., Haywood, M., et al. 2017, *A&A*, **604**, A106
- Korotin, S. A., Andrievsky, S. M., Hansen, C. J., et al. 2015, *A&A*, **581**, A70
- Kruijssen, J. M. D., Pfeffer, J. L., Chevance, M., et al. 2020, *MNRAS*, **498**, 2472
- Lawler, J. E., Bonvallet, G., & Sneden, C. 2001, *ApJ*, **556**, 452
- Lawler, J. E., Den Hartog, E. A., Sneden, C., & Cowan, J. J. 2006, *ApJS*, **162**, 227
- Li, R., Chatelain, R., Holt, R. A., et al. 2007, *Phys. Scr.*, **76**, 577
- Limberg, G., Santucci, R. M., Rossi, S., et al. 2021, *ApJ*, **913**, L28
- Limongi, M., & Chieffi, A. 2018, *ApJS*, **237**, 13
- Ljung, G., Nilsson, H., Asplund, M., & Johansson, S. 2006, *A&A*, **456**, 1181
- Lodders, K., Palme, H., & Gail, H. P. 2009, *Solar System, Landolt Börnstein*, **4B**, 712
- Malhan, K., Yuan, Z., Ibata, R. A., et al. 2021, *ApJ*, **920**, 51
- Mashonkina, L., Zhao, G., Gehren, T., et al. 2008, *A&A*, **478**, 529
- Mashonkina, L., Jablonka, P., Sitnova, T., Pakhomov, Y., & North, P. 2017, *A&A*, **608**, A89
- Matsuno, T., Koppelman, H. H., Helmi, A., et al. 2022, *A&A*, **661**, A103
- Matteucci, F., & Greggio, L. 1986, *A&A*, **154**, 279
- McWilliam, A. 1998, *AJ*, **115**, 1640
- Murphy, G. G., Yates, R. M., & Mohamed, S. S. 2022, *MNRAS*, **510**, 1945
- Myeong, G. C., Vasiliev, E., Iorio, G., Evans, N. W., & Belokurov, V. 2019, *MNRAS*, **488**, 1235
- Naidu, R. P., Conroy, C., Bonaca, A., et al. 2020, *ApJ*, **901**, 48
- Nishimura, N., Takiwaki, T., & Thielemann, F.-K. 2015, *ApJ*, **810**, 109
- Palmeri, P., Quinet, P., Wyart, J. F., & Biémont, E. 2000, *Phys. Scr.*, **61**, 323
- Placco, V. M., Sneden, C., Roederer, I. U., et al. 2021, *RNAAS*, **5**, 92
- Plez, B. 2012, *Astrophysics Source Code Library [record ascl:1205.004]*
- Plez, B., Brett, J. M., & Nordlund, Å. 1992, in *Instabilities in Evolved Super- and Hypergiants*, eds. C. de Jager, & H. Nieuwenhuijzen, 119
- Prantzos, N., Abia, C., Limongi, M., Chieffi, A., & Cristallo, S. 2018, *MNRAS*, **476**, 3432
- Rizzuti, F., Cescutti, G., Matteucci, F., et al. 2019, *MNRAS*, **489**, 5244
- Rizzuti, F., Cescutti, G., Matteucci, F., et al. 2021, *MNRAS*, **502**, 2495
- Roederer, I. U., Preston, G. W., Thompson, I. B., et al. 2014, *AJ*, **147**, 136
- Ryabchikova, T., Piskunov, N., Kurucz, R. L., et al. 2015, *Phys. Scr.*, **90**, 054005
- Sbordone, L., Caffau, E., Bonifacio, P., & Duffau, S. 2014, *A&A*, **564**, A109
- Schlafly, E. F., & Finkbeiner, D. P. 2011, *ApJ*, **737**, 103
- Simonetti, P., Matteucci, F., Greggio, L., & Cescutti, G. 2019, *MNRAS*, **486**, 2896
- Sneden, C., Lawler, J. E., Cowan, J. J., Ivans, I. I., & Den Hartog, E. A. 2009, *ApJS*, **182**, 80
- Suda, T., Katsuta, Y., Yamada, S., et al. 2008, *PASJ*, **60**, 1159
- Telting, J. H., Avila, G., Buchhave, L., et al. 2014, *Astron. Nachr.*, **335**, 41
- Villanova, S., Monaco, L., Geisler, D., et al. 2019, *ApJ*, **882**, 174
- Vincenzo, F., Spitoni, E., Calura, F., et al. 2019, *MNRAS*, **487**, L47
- Winteler, C., Käppeli, R., Perego, A., et al. 2012, *ApJ*, **750**, L22

## Appendix A: Line list

Table A.1. Line list

Elt	Ion	Wavelength	$\chi_{exc}$	$\log gf$
Sr	I	4607.327	0.000	+0.230
Y	II	4854.863	0.992	-0.380
Y	II	4883.684	1.084	0.070
Y	II	4900.120	1.033	-0.090
Y	II	5087.416	1.084	-0.170
Y	II	5119.112	0.992	-1.360
Y	II	5123.211	0.992	-0.830
Y	II	5200.406	0.992	-0.570
Y	II	5402.774	1.839	-0.510
Y	II	5662.925	1.944	0.160
Zr	II	4317.299	0.713	-1.450
Zr	II	4613.946	0.972	-1.540
Zr	II	5112.270	1.665	-0.850
Zr	II	5350.350	1.773	-1.160
La	II	4662.4774	0.000	-2.951
La	II	4662.4814	0.000	-2.511
La	II	4662.4852	0.000	-2.240
La	II	4662.4903	0.000	-2.252
La	II	4662.4914	0.000	-2.136
La	II	4662.4924	0.000	-2.256
La	II	4662.5024	0.000	-2.511
La	II	4662.5044	0.000	-2.056
La	II	4662.5063	0.000	-1.763
La	II	4920.976	0.126	-0.580
La	II	4921.776	0.244	-0.450
La	II	5114.5115	0.235	-1.624
La	II	5114.5284	0.235	-1.820
La	II	5114.5553	0.235	-1.820
La	II	5114.5723	0.235	-3.006
La	II	5114.5855	0.235	-1.824
La	II	5114.6073	0.235	-1.824
La	II	5114.6205	0.235	-2.079
La	II	5122.9798	0.321	-1.536
La	II	5122.9799	0.321	-2.106
La	II	5122.9859	0.321	-2.106
La	II	5122.9860	0.321	-1.934
La	II	5122.9864	0.321	-1.948
La	II	5122.9911	0.321	-1.948
La	II	5122.9915	0.321	-2.630
La	II	5122.9919	0.321	-1.959
La	II	5122.9954	0.321	-1.959
La	II	5122.9958	0.321	-4.059
La	II	5122.9962	0.321	-2.132
La	II	5122.9986	0.321	-2.132
La	II	5122.9990	0.321	-2.308
La	II	5290.818	0.000	-1.650
Ce	II	4539.853	1.645	-2.050
Ce	II	4562.282	1.327	-2.120
Ce	II	4628.161	0.516	0.200
Ce	II	5187.460	0.495	-2.300
Pr	II	5219.0096	0.795	-1.990
Pr	II	5219.0245	0.795	-1.943
Pr	II	5219.0382	0.795	-1.994
Pr	II	5219.0422	0.795	-0.720
Pr	II	5219.0507	0.795	-2.194
Pr	II	5219.0531	0.795	-0.794
Pr	II	5219.0629	0.795	-0.866

*continued on the next page*Table A.1. Line list (*continued*)

Elt	Ion	Wavelength	$\chi_{exc}$	$\log gf$
Pr	II	5219.0715	0.795	-0.934
Pr	II	5219.0789	0.795	-0.992
Pr	II	5219.0852	0.795	-1.035
Pr	II	5219.1018	0.795	-2.188
Pr	II	5219.1064	0.795	-1.990
Pr	II	5219.1099	0.795	-1.943
Pr	II	5219.1122	0.795	-1.994
Pr	II	5219.1134	0.795	-2.194
Pr	II	5220.0178	0.795	-3.464
Pr	II	5220.0339	0.795	-3.410
Pr	II	5220.0475	0.795	-1.892
Pr	II	5220.0486	0.795	-3.602
Pr	II	5220.0599	0.795	-1.693
Pr	II	5220.0711	0.795	-1.645
Pr	II	5220.0809	0.795	-1.696
Pr	II	5220.0894	0.795	-1.895
Pr	II	5220.0996	0.795	-0.368
Pr	II	5220.1071	0.795	-0.424
Pr	II	5220.1132	0.795	-0.481
Pr	II	5220.1181	0.795	-0.540
Pr	II	5220.1217	0.795	-0.598
Pr	II	5220.1239	0.795	-0.656
Pr	II	5259.6145	0.633	-3.727
Pr	II	5259.6329	0.633	-3.418
Pr	II	5259.6498	0.633	-3.356
Pr	II	5259.6653	0.633	-3.539
Pr	II	5259.6667	0.633	-1.961
Pr	II	5259.6789	0.633	-1.763
Pr	II	5259.6897	0.633	-1.716
Pr	II	5259.6991	0.633	-1.767
Pr	II	5259.7070	0.633	-1.965
Pr	II	5259.7251	0.633	-0.538
Pr	II	5259.7312	0.633	-0.603
Pr	II	5259.7358	0.633	-0.669
Pr	II	5259.7390	0.633	-0.737
Pr	II	5259.7408	0.633	-0.806
Pr	II	5259.7411	0.633	-0.874
Pr	II	5322.6702	0.482	-3.392
Pr	II	5322.6704	0.482	-3.320
Pr	II	5322.6714	0.482	-3.710
Pr	II	5322.6718	0.482	-3.488
Pr	II	5322.7044	0.482	-2.073
Pr	II	5322.7102	0.482	-1.878
Pr	II	5322.7173	0.482	-1.826
Pr	II	5322.7257	0.482	-1.871
Pr	II	5322.7297	0.482	-1.164
Pr	II	5322.7354	0.482	-2.066
Pr	II	5322.7427	0.482	-1.082
Pr	II	5322.7571	0.482	-0.998
Pr	II	5322.7727	0.482	-0.915
Pr	II	5322.7897	0.482	-0.836
Pr	II	5322.8079	0.482	-0.760
Pr	II	6165.891	0.923	-0.299
Nd	II	4501.810	0.205	-0.690
Nd	II	4859.026	0.321	-0.440
Nd	II	4959.115	0.064	-0.800
Nd	II	5076.580	0.742	-0.386
Nd	II	5255.502	0.205	-0.670
Nd	II	5293.160	0.823	0.100
Nd	II	5319.810	0.550	-0.140

*continued on the next page*

**Table A.1.** Line list (*continued*)

Elt	Ion	Wavelength	$\chi_{exc}$	$\log gf$
Sm	II	4566.200	0.333	-0.590
Sm	II	4615.440	0.544	-0.690
Sm	II	4669.640	0.277	-0.530
Sm	II	4674.590	0.185	-0.560
Sm	II	4676.900	0.040	-0.870
Sm	II	4791.579	0.104	-1.440
Sm	II	4913.259	0.659	-0.930
Eu	II	4435.4571	0.207	-0.696
Eu	II	4435.4650	0.207	-1.708
Eu	II	4435.4725	0.207	-3.034
Eu	II	4435.5254	0.207	-0.816
Eu	II	4435.5329	0.207	-1.525
Eu	II	4435.5395	0.207	-2.689
Eu	II	4435.5823	0.207	-0.947
Eu	II	4435.5889	0.207	-1.491
Eu	II	4435.5944	0.207	-2.577
Eu	II	4435.6273	0.207	-1.093
Eu	II	4435.6328	0.207	-1.550
Eu	II	4435.6369	0.207	-2.689
Eu	II	4435.6602	0.207	-1.256
Eu	II	4435.6643	0.207	-1.733
Eu	II	4435.6808	0.207	-1.432
Eu	II	4522.4767	0.207	-2.159
Eu	II	4522.4887	0.207	-1.266
Eu	II	4522.5292	0.207	-1.984
Eu	II	4522.5394	0.207	-1.474
Eu	II	4522.5515	0.207	-2.159
Eu	II	4522.5724	0.207	-1.962
Eu	II	4522.5806	0.207	-1.711
Eu	II	4522.5908	0.207	-1.984
Eu	II	4522.6064	0.207	-2.038
Eu	II	4522.6123	0.207	-1.980
Eu	II	4522.6205	0.207	-1.962
Eu	II	4522.6312	0.207	-2.247
Eu	II	4522.6349	0.207	-2.256
Eu	II	4522.6408	0.207	-2.038
Eu	II	4522.6483	0.207	-2.344
Eu	II	4522.6520	0.207	-2.247
Eu	II	6645.0727	1.379	-1.823
Eu	II	6645.0744	1.379	-0.517
Eu	II	6645.0749	1.379	-3.452
Eu	II	6645.0876	1.379	-0.593
Eu	II	6645.0898	1.379	-1.628
Eu	II	6645.0945	1.379	-3.151
Eu	II	6645.0974	1.379	-0.672
Eu	II	6645.1021	1.379	-1.583
Eu	II	6645.1047	1.379	-0.755
Eu	II	6645.1081	1.379	-3.079
Eu	II	6645.1101	1.379	-0.839
Eu	II	6645.1107	1.379	-1.635
Eu	II	6645.1144	1.379	-0.921
Eu	II	6645.1164	1.379	-1.830
Eu	II	6645.1170	1.379	-3.236

**Table A.2.** Barium Line list

Elt	Ion	Isotope	Wavelength	$\chi_{exc}$	$\log gf$
Ba	II	134	4554.034	0.000	+0.170
Ba	II	134	4934.100	0.000	-1.157
Ba	II	134	5853.690	0.604	-1.010
Ba	II	134	6141.730	0.704	-0.077
Ba	II	134	6496.910	0.604	-0.380
Ba	II	135	4554.003	0.000	-0.636
Ba	II	135	4554.004	0.000	-1.033
Ba	II	135	4554.004	0.000	-0.636
Ba	II	135	4554.050	0.000	-0.189
Ba	II	135	4554.053	0.000	-0.636
Ba	II	135	4554.054	0.000	-1.337
Ba	II	135	4934.059	0.000	-1.662
Ba	II	135	4934.070	0.000	-2.362
Ba	II	135	4934.118	0.000	-1.662
Ba	II	135	4934.129	0.000	-1.662
Ba	II	135	5853.687	0.604	-2.066
Ba	II	135	5853.688	0.604	-2.009
Ba	II	135	5853.689	0.604	-2.215
Ba	II	135	5853.690	0.604	-2.620
Ba	II	135	5853.690	0.604	-1.914
Ba	II	135	5853.690	0.604	-1.466
Ba	II	135	5853.691	0.604	-2.215
Ba	II	135	5853.693	0.604	-2.009
Ba	II	135	5853.694	0.604	-2.066
Ba	II	135	6141.725	0.704	-2.456
Ba	II	135	6141.727	0.704	-1.311
Ba	II	135	6141.728	0.704	-2.284
Ba	II	135	6141.729	0.704	-1.214
Ba	II	135	6141.729	0.704	-0.503
Ba	II	135	6141.731	0.704	-1.327
Ba	II	135	6141.731	0.704	-0.709
Ba	II	135	6141.732	0.704	-1.281
Ba	II	135	6141.732	0.704	-0.959
Ba	II	135	6496.899	0.604	-1.886
Ba	II	135	6496.902	0.604	-1.186
Ba	II	135	6496.906	0.604	-0.739
Ba	II	135	6496.916	0.604	-1.583
Ba	II	135	6496.917	0.604	-1.186
Ba	II	135	6496.920	0.604	-1.186
Ba	II	136	4554.034	0.000	+0.170
Ba	II	136	4934.100	0.000	-1.157
Ba	II	136	5853.690	0.604	-1.010
Ba	II	136	6141.730	0.704	-0.077
Ba	II	136	6496.910	0.604	-0.380
Ba	II	137	4554.001	0.000	-0.636
Ba	II	137	4554.002	0.000	-1.033
Ba	II	137	4554.002	0.000	-0.636
Ba	II	137	4554.053	0.000	-0.189
Ba	II	137	4554.056	0.000	-0.636
Ba	II	137	4554.057	0.000	-1.337
Ba	II	137	4934.054	0.000	-1.662
Ba	II	137	4934.066	0.000	-2.362
Ba	II	137	4934.121	0.000	-1.662
Ba	II	137	4934.132	0.000	-1.662
Ba	II	137	5853.686	0.604	-2.066
Ba	II	137	5853.687	0.604	-2.009
Ba	II	137	5853.689	0.604	-2.215

*continued on the next page*

**Table A.2.** Barium Line list (*continued*)

Elt	Ion	Isotope	Wavelength	$\chi_{exc}$	$\log gf$
Ba	II	137	5853.690	0.604	-2.620
Ba	II	137	5853.690	0.604	-1.914
Ba	II	137	5853.690	0.604	-1.466
Ba	II	137	5853.692	0.604	-2.215
Ba	II	137	5853.693	0.604	-2.009
Ba	II	137	5853.694	0.604	-2.066
Ba	II	137	6141.725	0.704	-2.456
Ba	II	137	6141.727	0.704	-1.311
Ba	II	137	6141.728	0.704	-2.284
Ba	II	137	6141.729	0.704	-1.214
Ba	II	137	6141.729	0.704	-0.503
Ba	II	137	6141.731	0.704	-1.327
Ba	II	137	6141.731	0.704	-0.709
Ba	II	137	6141.732	0.704	-0.959
Ba	II	137	6141.733	0.704	-1.281
Ba	II	137	6496.898	0.604	-1.886
Ba	II	137	6496.901	0.604	-1.186
Ba	II	137	6496.906	0.604	-0.739
Ba	II	137	6496.916	0.604	-1.583
Ba	II	137	6496.918	0.604	-1.186
Ba	II	137	6496.922	0.604	-1.186
Ba	II	138	4554.036	0.000	+0.170
Ba	II	138	4934.100	0.000	-1.157
Ba	II	138	5853.690	0.604	-1.010
Ba	II	138	6141.730	0.704	-0.077
Ba	II	138	6496.910	0.604	-0.380

Table A.3. Abundances

Star	[Fe1/H]	$\sigma$ (Fe1)	[Fe2/H]	$\sigma$ (Fe2)	[Sr/H]	$\sigma$ (Sr)	[Y/H]	$\sigma$ (Y)	[Zr/H]	$\sigma$ (Zr)	[Ba/H]	$\sigma$ (Ba)
Sequoia												
HD115575	-1.99	0.09	-1.86	0.12	-2.40	0.00	-2.16	0.05	-1.53	0.04	-2.16	0.08
TYC 4267-2023-1	-1.74	0.14	-2.08	0.16	-1.65	0.05	-1.91	0.08	-1.36	0.09	-1.70	0.09
BD+31 2143	-2.36	0.10	-2.24	0.12	-2.30	0.16	-2.45	0.03	-1.98	0.05	-2.42	0.00
GSE												
BD+20 3298	-1.95	0.10	-1.86	0.17	-2.23	0.13	-2.12	0.05	-1.55	0.03	-1.83	0.02
TYC 1008-1200-1	-2.23	0.10	-2.00	0.17	-2.45	0.05	-2.24	0.06	-1.77	0.10	-2.00	0.05
HD 238439	-2.09	0.11	-2.02	0.13	-2.40	0.00	-2.12	0.04	-1.58	0.04	-1.98	0.09
HD 142614	-1.45	0.11	-1.47	0.18	-1.80	0.00	-1.46	0.06	-0.86	0.02	-1.15	0.10
BD +04 18	-1.48	0.12	-1.28	0.31	-1.90	0.00	-1.31	0.06	-0.80	0.04	-0.78	0.04
BD+39 3309	-2.58	0.13	-2.46	0.13	-2.30	0.00	-2.57	0.02	—	—	-3.02	0.07
TYC 2824-1963-1	-1.60	0.14	-1.45	0.38	-2.15	0.00	-1.63	0.08	-1.08	0.02	-1.23	0.00
TYC 4001-1161-1	-1.62	0.11	-1.28	0.29	-2.15	0.00	-1.69	0.06	-1.05	0.06	-1.23	0.03
TYC 4221-640-1	-2.27	0.11	-2.19	0.22	-2.70	0.00	-2.52	0.04	-1.94	0.05	-2.56	0.06
TYC 4-369-1	-1.84	0.11	-1.66	0.25	-2.25	0.00	-1.84	0.06	-1.32	0.05	-1.60	0.00
other												
BD -00 4538	-1.90	0.09	-1.75	0.14	-2.00	0.12	-1.98	0.05	-1.43	0.04	-1.73	0.05
BD +03 4904	-2.57	0.12	-2.47	0.17	-2.53	0.03	-2.65	0.06	-1.97	0.00	-2.86	0.06
BD +07 4625	-1.93	0.10	-1.92	0.13	-2.28	0.06	-2.19	0.04	-1.64	0.06	-1.94	0.00
BD+11 2896	-1.41	0.12	-1.30	0.20	-1.70	0.10	-1.49	0.06	-0.90	0.04	-1.25	0.00
BD +21 4759	-2.50	0.14	-2.34	0.12	-2.40	0.00	-2.27	0.04	-1.82	0.04	-1.98	0.03
BD +25 4520	-2.28	0.10	-2.13	0.17	-2.52	0.16	-2.68	0.05	-1.94	0.06	-2.61	—
BD +32 2483	-2.25	0.11	-2.20	0.16	-2.35	0.05	-2.38	0.05	-1.82	0.04	-2.42	0.04
BD +35 4847	-1.91	0.10	-1.90	0.17	-1.80	0.00	-1.62	0.04	-1.25	0.06	-1.43	0.06
BD +48 2167	-2.28	0.11	-2.15	0.12	-1.95	0.10	-2.43	0.04	-1.90	0.02	-2.20	0.04
BD -07 3523	-1.95	0.10	-1.87	0.16	-2.35	0.00	-2.04	0.04	-1.52	0.05	-1.73	0.10
BD +06 2880	-1.45	0.11	-1.30	0.23	-1.85	0.15	-1.53	0.04	-0.98	0.02	-1.00	0.02
HD 139423	-1.70	0.11	-1.78	0.15	-2.05	0.00	-1.84	0.07	-1.23	0.04	-1.71	0.07
HD 208316	-1.61	0.10	-1.57	0.10	-1.85	0.00	-1.52	0.04	-1.00	0.03	-1.53	0.04
HD 354750	-2.35	0.11	-2.42	0.14	-2.25	0.05	-2.54	0.03	—	—	-2.53	0.02
TYC 2588-1386-1	-1.73	0.12	-1.70	0.20	-2.20	0.00	-1.79	0.06	-1.28	0.02	-1.50	0.07
TYC 3085-119-1 <sup>a</sup>	-1.51	0.10	-1.42	0.17	-1.31	0.07	-1.24	0.06	-0.78	0.07	-1.07	0.05
TYC 33-446-1	-2.22	0.12	-2.20	0.20	-2.38	0.03	-2.37	0.06	-1.70	0.05	-2.15	0.06
TYC 3944-698-1	-2.18	0.13	-2.06	0.21	-2.70	0.00	-2.26	0.07	-1.79	0.02	-2.26	0.04
TYC 4331-136-1	-2.53	0.11	-2.43	0.23	-2.75	0.00	-2.62	0.07	-1.92	0.05	-2.58	0.02
TYC 4584-784-1	-2.03	0.11	-1.85	0.25	-2.35	0.00	-2.11	0.08	-1.49	0.06	-1.90	0.00

<sup>a</sup> Thick-disc star

**Table A.3.** Abundances (continued).

Star	[La/H]	$\sigma(\text{La})$	[Ce/H]	$\sigma(\text{Ce})$	[Pr/H]	$\sigma(\text{Pr})$	[Nd/H]	$\sigma(\text{Nd})$	[Sm/H]	$\sigma(\text{Sm})$	[Eu/H]	$\sigma(\text{Eu})$
Sequoia												
HD115575	-2.06	0.06	-2.19	0.06	-2.17	0.04	-2.02	0.03	-1.84	0.05	-1.83	0.00
TYC 4267-2023-1	-1.64	0.07	-1.81	0.07	-1.74	0.09	-1.61	0.05	-1.47	0.04	-1.43	0.00
BD+31 2143	-2.42	0.05	-2.50	0.04	-2.19	0.08	-2.37	0.05	-2.10	0.04	-2.23	0.00
GSE												
BD+20 3298	-1.77	0.05	-1.96	0.07	-1.53	0.10	-1.73	0.03	-1.55	0.09	-1.33	0.00
TYC 1008-1200-1	-2.01	0.04	-2.20	0.04	-1.95	0.03	-1.93	0.04	-1.74	0.02	-1.68	0.05
HD 238439	-2.03	0.05	-2.15	0.11	-2.02	0.04	-2.01	0.04	-1.86	0.03	-1.63	0.00
HD 142614	-1.11	0.05	-1.34	0.07	-1.12	0.04	-1.07	0.05	-0.79	0.06	-0.68	0.05
BD +04 18	-0.90	0.05	-1.19	0.13	-0.62	0.09	-0.82	0.09	-0.57	0.06	-0.33	0.00
BD+39 3309	—	—	—	—	—	—	—	—	—	—	—	—
TYC 2824-1963-1	-1.28	0.04	-1.57	0.02	-1.22	0.04	-1.22	0.04	-1.00	0.10	-0.81	0.13
TYC 4001-1161-1	-1.39	0.08	-1.53	0.06	-1.36	0.06	-1.28	0.05	-1.04	0.12	-0.78	0.00
TYC 4221-640-1	-2.47	0.03	-2.63	0.08	-2.32	0.00	-2.29	0.07	-1.99	0.08	-1.78	0.00
TYC 4-369-1	-1.54	0.04	-1.67	0.05	-1.56	0.04	-1.47	0.05	-1.34	0.04	-1.26	0.07
other												
BD -00 4538	-1.65	0.03	-1.73	0.05	-1.50	0.06	-1.62	0.04	-1.37	0.03	-1.28	0.04
BD +03 4904	-2.61	0.02	-2.73	0.02	—	—	-2.52	0.04	-2.01	0.05	—	—
BD +07 4625	-1.75	0.07	-1.89	0.04	—	0.19	-1.71	0.05	-1.52	0.04	-1.53	0.00
BD+11 2896	-1.13	0.07	-1.38	0.07	-0.92	0.12	-1.05	0.02	-0.80	0.11	-0.63	0.00
BD +21 4759	-1.85	0.03	-2.07	0.06	—	0.06	-1.73	0.05	-1.47	0.05	-1.23	0.00
BD +25 4520	-2.50	0.04	-2.72	0.10	—	—	-2.43	0.04	-2.16	0.05	—	—
BD +32 2483	-2.28	0.04	-2.45	0.04	-2.12	0.05	-2.22	0.04	-2.04	0.06	—	—
BD +35 4847	-1.43	0.08	-1.69	0.05	-1.38	0.08	-1.56	0.05	-1.45	0.06	-1.33	0.00
BD +48 2167	-2.22	0.04	-2.38	0.06	-1.97	0.10	-2.21	0.06	-1.93	0.08	-1.78	0.00
BD -07 3523	-1.71	0.02	-1.88	0.06	-1.45	0.10	-1.61	0.04	-1.42	0.03	-1.18	0.00
BD +06 2880	-1.15	0.04	-1.48	0.10	-1.03	0.10	-1.10	0.06	-0.95	0.05	-0.78	0.04
HD 139423	-1.49	0.04	-1.72	0.02	-1.41	0.04	-1.39	0.04	-1.18	0.02	-1.13	0.05
HD 208316	-1.49	0.04	-1.68	0.09	-1.51	0.04	-1.47	0.04	-1.30	0.05	-1.13	0.00
HD 354750	-2.26	0.05	-2.53	0.08	—	—	-2.16	0.05	-1.94	0.06	-1.83	0.00
TYC 2588-1386-1	-1.47	0.06	-1.69	0.13	-1.52	0.04	-1.41	0.07	-1.24	0.03	-1.13	0.00
TYC 3085-119-1 <sup>a</sup>	-1.04	0.03	-1.19	0.07	-1.15	0.02	-1.11	0.04	-0.93	0.06	-0.88	0.05
TYC 33-446-1	-2.04	0.05	-2.15	0.04	-1.97	0.08	-1.93	0.03	-1.86	0.07	-0.58	1.05
TYC 3944-698-1	-2.20	0.02	-2.33	0.05	-2.02	0.00	-2.16	0.03	-1.94	0.08	-1.63	0.00
TYC 4331-136-1	-2.34	0.03	-2.57	0.06	-2.32	0.04	-2.29	0.06	-2.02	0.04	-1.78	0.05
TYC 4584-784-1	-1.76	0.06	-1.94	0.08	-1.70	0.05	-1.72	0.04	-1.55	0.05	-1.38	0.05

<sup>a</sup> Thick-disc star